

Minimum Reduced-Order Models via Causal Inference

Nan Chen¹ and Honghu Liu²

¹Department of Mathematics, University of Wisconsin-Madison, Madison, WI 53705, USA
(chenan@math.wisc.edu)

²Department of Mathematics, Virginia Tech, Blacksburg, VA 24061, USA (hhliu@vt.edu)

June 28, 2024

Abstract

Enhancing the sparsity of data-driven reduced-order models (ROMs) has gained increasing attention in recent years. In this work, we analyze an efficient approach to identifying skillful ROMs with a sparse structure using an information-theoretic indicator called causation entropy. The causation entropy quantifies in a statistical way the additional contribution of each term to the underlying dynamics beyond the information already captured by all the other terms in the ansatz. By doing so, the causation entropy assesses the importance of each term to the dynamics before a parameter estimation procedure is performed. Thus, the approach can be utilized to eliminate terms with little dynamic impact, leading to a parsimonious structure that retains the essential physics. To circumvent the difficulty of estimating high-dimensional probability density functions (PDFs) involved in the causation entropy computation, we leverage Gaussian approximations for such PDFs, which are demonstrated to be sufficient even in the presence of highly non-Gaussian dynamics. The effectiveness of the approach is illustrated by the Kuramoto-Sivashinsky equation by building sparse causation-based ROMs for various purposes, such as recovering long-term statistics and inferring unobserved dynamics via data assimilation with partial observations.

Contents

1	Introduction	2
2	A Causation-Based ROM Framework	4
2.1	Overview	4
2.2	Determining model structure using a causation inference	5
2.2.1	Determining the state variables	5
2.2.2	Developing a function library	6
2.2.3	Computing the causation entropy	6
2.2.4	Parameter estimation	8

3	Reduced-Order Models for the Kuramoto-Sivashinsky Equation based on Causal Inference	8
3.1	Preliminaries and background	8
3.1.1	Galerkin projections of the KSE under the Fourier basis	9
3.1.2	Galerkin projections of the KSE under the POD basis	10
3.1.3	Parameter regime and numerical setup	11
3.2	Data-driven inverse models under the Fourier basis	11
3.3	Data-driven inverse models under the POD basis	16
3.4	Application to data assimilation with partial observations	19
4	Discussion and Conclusions	22

Constructing sparse, effective reduced-order models (ROMs) for high-dimensional dynamical data is a crucial area of research in applied sciences. For observational or synthetic time series generated by nonlinear chaotic dynamical systems, a direct application of nonlinear regressions to fit a comprehensive model ansatz typically leads to non-zero coefficients for a high percentage of the terms. Eliminating the terms with weak contributions to the dynamics is crucial for gaining computation efficiency and enhancing model interpretability. This work demonstrates the effectiveness of an information-theoretic concept called causation entropy in ranking the importance of each candidate term in a given ansatz to the underlying dynamics. Using the Kuramoto-Sivashinsky equation, a well-known example of spatiotemporal chaos, we demonstrate that causation-based ROMs can near-perfectly capture the sparse structure of the true projected model when represented using a Fourier basis. Even when the true projected model does not necessarily possess a sparse structure under a chosen basis, a hierarchy of causation-based ROMs with different degrees of sparsity is shown to be skillful for various tasks, such as recovering long-term statistics and inferring unobserved dynamics via data assimilation with partial observations.

1 Introduction

Complex dynamical systems appear in many scientific areas, including climate science, geophysics, engineering, neuroscience, plasma physics, and material science [36, 75, 82, 88, 90]. They play a vital role in describing the underlying physics and facilitating the study of many important issues, such as state estimation and forecasting. However, direct numerical simulation is often quite expensive due to the high dimensionality and the multiscale nature of these systems. The situation becomes even more computationally prohibitive when ensemble methods, such as ensemble data assimilation and statistical forecast, are applied to these systems. Therefore, developing appropriate reduced-order models (ROMs) becomes essential not only to reduce the computational cost but also to discover the dominant dynamics of the underlying system.

Many of the ROMs have explicit mathematical expressions. On the one hand, when the complex nonlinear governing equations of the full system are given, one systematic approach to developing ROMs is to project the starting model to the leading a few energetic modes. Commonly used projection techniques include the Galerkin proper orthogonal decomposition [41], the dynamic mode decomposition [69, 73], the principal interaction patterns [39, 51] and methods based on other

empirical basis functions. Once the projection is implemented, supplementing the resulting equations with closure terms is often essential to compensate for the truncation error [13, 63, 84, 92]. On the other hand, many data-driven methods have been developed to learn the dynamics from the observed or simulated data associated with the large-scale features or dominant modes of the full systems [1, 12, 20, 26, 40, 55, 61, 67, 79]. The full system does not necessarily need to be known in such a case. It is worth mentioning that there are many recent developments in non-parametric ROMs or surrogate models, including those resulting from machine learning methods [14–17, 19, 21, 23, 24, 27, 60, 62, 66, 70, 80, 89]. Many of these developments focus primarily on providing efficient forecast results. At the same time, less effort is spent on finding physically explainable parametric expressions.

When the ROMs are given by parametric forms, it is often expected that the model is not only simple enough to facilitate the computations but also skillful in describing the underlying physics. Notably, these two issues are related; a physically explainable model usually has a parsimonious structure. As the underlying full system is nonlinear, the resulting ROM from a certain projection method often contains a large number of nonlinear terms. Similarly, starting with a comprehensive nonlinear model ansatz, applying the standard nonlinear regression to the observed time series typically leads to a high percentage of the terms with non-zero coefficients. Eliminating the terms with weak contributions to the dynamics is crucial in providing a simple and explainable model. One straightforward way to build a ROM with sparsity is first to rank the coefficients of the model and then remove the terms with small coefficients. However, the dynamical contribution is not simply characterized by the amplitude of the coefficients or even the energy of the associated terms. For chaotic systems, removing the terms with even a tiny amount of energy can sometimes cause a strong regime switching and bring about completely different dynamics in the resulting ROMs [32]. Therefore, systematic sparse identification becomes essential to find a parsimonious model. The least absolute shrinkage and selection operator (LASSO) regression [71, 85] has been widely used or incorporated into a certain optimization procedure for the selection of terms [9, 12, 30, 72, 74]. By pre-determining the degree of shrinkage (i.e., the level of the regularization), the LASSO regression leads to a ROM with a sparse structure. It has provided many successful results, especially in discovering models from data.

Yet, beyond the sparsity of the model structure, there are several crucial issues in obtaining a physics-informed parsimonious ROM. First, it is of practical significance to seek a quantitative indicator that assesses the importance of each term in the starting model contributing to the underlying dynamics. It can be utilized as systematic guidance to eliminate redundant terms that have little impact on the dynamics, leading to a parsimonious structure that retains the essential physics. By gradually dropping the terms based on their relevance to the underlying dynamics using this indicator, the procedure also facilitates identifying the tipping point terms in the resulting ROM, excluding which will trigger regime switching or lead to biased statistics. In other words, such an indicator advances a physics-informed minimum ROM. Although the importance of each term in the starting model can be ranked by repeatedly applying the LASSO regression with different degrees of shrinkage, the total computation in such a brute-force method is costly. Second, the truncation error or model uncertainty represented by random noises can affect the learning outcome using many purely data-driven methods. It has been shown that, in the presence of even slight random noise, both the covariate selection accuracy and the fraction of zero entries may decrease significantly [33] when applying the standard LASSO regression, leading to a large bias in describing the underlying physics. This requires a robust sparse identification method barely

affected by the stochastic noise.

In this paper, a computationally efficient model identification method based on causal inference [2,3,33–35,46] is utilized for developing minimum ROMs and exploring its skill in prediction, data assimilation and capturing the crucial features of the underlying system. A so-called causation entropy is introduced as the quantitative indicator that advances the discovery of the physics-informed minimum ROM. The causation entropy measures the additional contribution of each term to the underlying dynamics beyond the information contained in all the other candidates. Previous studies illustrated that causation entropy as well as other related variants are appropriate surrogates for characterizing the significant physics represented by each candidate term [3, 28, 33, 46], and these information-theoretic criteria can lead to better sparse ROMs than those constructed from metric-based minimization techniques [3]. Causation entropy has also been shown to be insensitive to perturbations of the signal due to external random noise [33]. Therefore, it can play a vital role in providing robust results for model identification. Indeed, as will be shown in Sec. 3 on the Kuramoto-Sivashinsky equation [50, 77], the resulting physics-informed minimum ROM not only captures the underlying physics but also reproduces crucial statistics of the studied model. Moreover, as causal inference is utilized to identify the coupled relationship between different model components, the ROM is appropriate in providing accurate state estimation results when the Bayesian inference is applied to study such an inverse problem. This desirable feature allows the model to be skillful in data assimilation with partial observations, as illustrated in Sec. 3.4.

The rest of the article is organized as follows. We first outline in Sec. 2 the general procedure to determine the causation-based ROMs, with the core concept of causation entropy and a computationally efficient approximation of this concept recalled in Sec. 2.2.3. The usefulness of this ROM framework is illustrated on the Kuramoto-Sivashinsky in Sec. 3 in the context of deriving sparse data-driven ROMs to capture either the long-term statistics of the solution or to recover unobserved dynamics using data assimilation. Some additional remarks and potential future directions are then provided in Sec. 4.

2 A Causation-Based ROM Framework

2.1 Overview

The causation-based ROM framework aims to exploit causal inference to develop ROMs that capture the underlying physics and have sparse model structures. Such a model identification method differs from the standard nonlinear regression approaches as the causal inference during the model identification process plays a significant role in determining the sparse ROMs. The method applies to both the knowledge-driven (meaning the full model is given) and data-driven scenarios. An overview of the modeling framework is as follows.

Step 1. Determine the dimension of the ROM.

Step 2. In the situation with the known parametric form of the full model, first, determine the basis functions used to project the full model. Then, write down the resulting projected model on these bases. When the only available information is data, determine a data-driven decomposition method and then project the data onto the associated basis functions to reach the time series.

- Step 3. Build a library of candidate functions as a prerequisite for model identification. These candidate functions are potential terms appearing on the right-hand side of one or a few equations of the ROM model. Physical knowledge can be used to assist the development of such a candidate set. The function library can also be built by including a large number of functions with arbitrary combinations of state variables that do not refer to any physical intuition.
- Step 4. A causal inference technique is utilized to reveal the underlying causal relationship between state variables and candidate functions. It plays a crucial role in determining the physically explainable parsimonious model structure.
- Step 5. A simple maximum likelihood method is adopted to estimate model parameters and characterize the model uncertainty by incorporating appropriate stochastic noises.

It is worthwhile highlighting several significant features of such a causation-based ROM framework. First, the method developed here fundamentally differs from a direct data-driven nonlinear regression method in determining the model structure. Typical nonlinear regression aims at minimizing a particular norm of the error. Therefore, the direct nonlinear regression method will end up with as many terms as possible on the right-hand side of the equation to account for the error reduction. Despite most of these terms with small coefficients being nonphysical, they cannot simply be set to zero since they may significantly contribute to the dynamics. Although LASSO-type regression methods can be applied to eliminate most candidate functions [71, 85], such a purely data-driven type method does not explicitly include any physics in the model identification. Notably, in the presence of slight random noise or chaotic trajectories, covariate selection accuracy and the fraction of zero entries may also decrease significantly [33]. In contrast, the causal inference exploits the causal relationship, which reflects the underlying physics, to automatically determine the model structure that provides a physically explainable parsimonious model [2, 3, 33–35, 46]. Second, analytic formulae are available to determine both the model structure via causation entropy and the parameters using maximum likelihood [22]. In other words, the causation-based ROM framework developed here is wholly explicit and highly efficient. It differs from many other machine learning methods that contain black boxes and require expensive training. Third, stochastic noise or stochastic parameterizations can automatically be incorporated into this framework. Oftentimes, nonlinear stochastic terms are crucial for the resulting models to reproduce irregular features and recover many observed statistics, which can be more challenging to achieve by purely deterministic models. These stochastic terms also describe model uncertainty, a crucial part of the stochastic conceptual models.

2.2 Determining model structure using a causation inference

2.2.1 Determining the state variables

The state variables of the ROM in this causation-based learning framework are pre-determined. These variables are denoted by an n -dimensional column vector $\mathbf{U} = (u_1, \dots, u_n)^T$, where each u_i is one state variable.

2.2.2 Developing a function library

After determining the state variables of the ROM, a library \mathbf{f} consisting of in total M possible candidate functions to describe the right-hand side of the model is developed,

$$\mathbf{f} = \{f_1, \dots, f_{m-1}, f_m, f_{m+1}, \dots, f_M\}. \quad (1)$$

Typically, a large number of candidate functions is included in the library to allow for coverage over different possible dynamical features of the underlying true dynamics. Each f_m is given by a linear or nonlinear function containing a few components of \mathbf{U} . Prior knowledge of the dynamics can help determine the function library. The library can also include as many potential candidate functions as possible, allowing the causal inference to determine the useful ones automatically.

2.2.3 Computing the causation entropy

Next, causal inference is utilized to determine the model structure. To this end, a causation entropy $C_{f_m \rightarrow \dot{u}_i | [\mathbf{f} \setminus f_m]}$ is computed to detect if the candidate function f_m contributes to the right-hand side of the equation for u_i , namely $du_i/dt := \dot{u}_i$. The causation entropy is given by [2, 3, 34, 46]:

$$C_{f_m \rightarrow \dot{u}_i | [\mathbf{f} \setminus f_m]} = H(\dot{u}_i | [\mathbf{f} \setminus f_m]) - H(\dot{u}_i | \mathbf{f}), \quad (2)$$

where $\mathbf{f} \setminus f_m$ represent the set that contains all functions in \mathbf{f} except f_m . In other words, $\mathbf{f} \setminus f_m$ contains $M - 1$ candidate functions and is defined as

$$\mathbf{f} \setminus f_m = \{f_1, \dots, f_{m-1}, f_{m+1}, \dots, f_M\}. \quad (3)$$

The term $H(\cdot | \cdot)$ is the conditional entropy, which is related to Shannon's entropy $H(\cdot)$ and the joint entropy $H(\cdot, \cdot)$. For two multi-dimensional random variables \mathbf{X} and \mathbf{Y} (with the corresponding states being \mathbf{x} and \mathbf{y}), they are defined as [31]:

$$\begin{aligned} H(\mathbf{X}) &= - \int_{\mathbf{x}} p(\mathbf{x}) \log(p(\mathbf{x})) \, d\mathbf{x}, \\ H(\mathbf{Y} | \mathbf{X}) &= - \int_{\mathbf{x}} \int_{\mathbf{y}} p(\mathbf{x}, \mathbf{y}) \log(p(\mathbf{y} | \mathbf{x})) \, d\mathbf{y} \, d\mathbf{x}, \\ H(\mathbf{X}, \mathbf{Y}) &= - \int_{\mathbf{x}} \int_{\mathbf{y}} p(\mathbf{x}, \mathbf{y}) \log(p(\mathbf{x}, \mathbf{y})) \, d\mathbf{y} \, d\mathbf{x}, \end{aligned} \quad (4)$$

where $p(\mathbf{x})$ is the probability density function (PDF) of \mathbf{x} and $p(\mathbf{y} | \mathbf{x})$ is the conditional PDF of \mathbf{y} given \mathbf{x} . On the right-hand side of (2), the difference between the two conditional entropies indicates the information in \dot{u}_i contributed by the specific function f_m given the contributions from all the other functions. Thus, it tells if f_m provides additional information to \dot{u}_i conditioned on the other potential terms in the dynamics. Note also that the causation entropy $C_{f_m \rightarrow \dot{u}_i | [\mathbf{f} \setminus f_m]}$ actually coincides with the conditional mutual information of \dot{u}_i and f_m given $\mathbf{f} \setminus f_m$, usually denoted by $I(\dot{u}_i; f_m | \mathbf{f} \setminus f_m)$, which is always non-negative [31, Sec. 2.5]. It is also worthwhile to highlight that the causation entropy in (2) is fundamentally different from directly computing the correlation between \dot{u}_i and f_m , as the causation entropy also considers the influence of the other library functions. If both \dot{u}_i and f_m are caused by a common factor $f_{m'}$, then \dot{u}_i and f_m can be highly

correlated. Yet, in such a case, the causation entropy $C_{f_m \rightarrow \dot{u}_i | [\mathbf{f} \setminus f_m]}$ will be close to zero as f_m is not the causation of \dot{u}_i .

The causation entropy is computed from each of the candidate functions in \mathbf{f} to each \dot{u}_i . Thus, there are in total nM causation entropies, which can be written as an $n \times M$ matrix, called the causation entropy matrix. Note that the dimension \mathbf{X} in (4) is M when it is applied to compute the second term on the right-hand side of the causation entropy in (2). This implies that the direct calculation of the entropies in (4) involves a high-dimensional numerical integration, which is a well-known computationally challenging issue [5]. To circumvent the direct numerical integration, the entropy calculation approximates all the joint and marginal distributions as Gaussians. In such a way, the causation entropy can be computed by

$$\begin{aligned} C_{\mathbf{Z} \rightarrow \mathbf{X} | \mathbf{Y}} &= H(\mathbf{X} | \mathbf{Y}) - H(\mathbf{X} | \mathbf{Y}, \mathbf{Z}) \\ &= H(\mathbf{X}, \mathbf{Y}) - H(\mathbf{Y}) - H(\mathbf{X}, \mathbf{Y}, \mathbf{Z}) + H(\mathbf{Y}, \mathbf{Z}) \\ &\approx \frac{1}{2} \ln(\det(\mathbf{R}_{\mathbf{XY}})) - \frac{1}{2} \ln(\det(\mathbf{R}_{\mathbf{Y}})) - \frac{1}{2} \ln(\det(\mathbf{R}_{\mathbf{XYZ}})) + \frac{1}{2} \ln(\det(\mathbf{R}_{\mathbf{YZ}})), \end{aligned} \quad (5)$$

where $\mathbf{R}_{\mathbf{XYZ}}$ denotes the covariance matrix of the state variables $(\mathbf{X}, \mathbf{Y}, \mathbf{Z})$ and similar for other covariances. The notations $\ln(\cdot)$ and $\det(\cdot)$ are the logarithm of a number and determinant of a matrix, respectively.

The simple and explicit expression in (5) based on the Gaussian approximation can efficiently compute the causation entropy. It allows the computation of the causation entropy with a moderately large dimension, sufficient for deriving conceptual models. It is worth noting that the Gaussian approximation may lead to certain errors in computing the causation entropy if the true distribution is highly non-Gaussian. Nevertheless, the primary goal is not to obtain the exact value of the causation entropy. Instead, it suffices to detect if the causation entropy $C_{f_m \rightarrow \dot{u}_i | [\mathbf{f} \setminus f_m]}$ is nonzero (or practically above a small threshold value). In most applications, if a significant causal relationship is detected in the higher-order moments, it is very likely in the Gaussian approximation. This allows us to efficiently determine the sparse model structure, where the exact values of the nonzero coefficients on the right-hand side of the model will be calculated via a simple maximum likelihood estimation to be discussed in the following. Note that the Gaussian approximation has been widely applied to compute various information measurements and leads to reasonably accurate results [11, 47, 58, 86].

With the $n \times M$ causation entropy matrix in hand, the next step is determining the model structure. This can be done by setting up a threshold value of the causation entropy and retaining only those candidate functions with the causation entropies exceeding the threshold. Alternatively, the importance of each candidate function can be ranked using the causation entropy, and only a certain percentage of the terms on top of this list is retained. This allows the resulting model to contain only functions that significantly contribute to the dynamics and facilitates a sparse model structure. Sparsity is crucial to discovering the correct underlying physics and prevents overfitting [12, 93]. It will also guarantee the robustness of the model in response to perturbations and allow the model to apply to certain extrapolation tests. Notably, determining the importance of the terms using the causation entropy fundamentally differs from that by first ranking the absolute strength of the regression coefficients of the model and then removing the terms with small coefficients. The latter does not explicitly consider the dynamical contributions and can be biased in leading to a very different sparse ROM.

2.2.4 Parameter estimation

The final step is to estimate the parameters in the resulting model. The model of \mathbf{U} can be written in the vector form:

$$\frac{d\mathbf{U}}{dt} = \Phi(\mathbf{U}) + \sigma \dot{\mathbf{W}}(t), \quad (6)$$

where $\Phi(\mathbf{U})$ is an n -dimensional column vector with each entry representing the summation of the selected nonlinear candidate functions from the causal inference for each component of \mathbf{U} . The matrix $\sigma \in \mathbb{R}^{n \times d}$ is the noise amplitude, and $\dot{\mathbf{W}}(t) \in \mathbb{R}^{d \times 1}$ is a white noise.¹ Denote by $\Theta \in \mathbb{R}^s$ a column vector containing all the parameters in the model with $s \gg n$ in a typical situation. The first term on the right-hand side of (6) can be written as

$$\Phi(\mathbf{U}) = \mathbf{M}\Theta + \mathbf{Q}, \quad (7)$$

where $\mathbf{M} \in \mathbb{R}^{n \times s}$ is a matrix, each entry of which is a function of \mathbf{U} contained in the predefined library \mathbf{f} given by (1) while $\mathbf{Q} \in \mathbb{R}^n$ is a column vector that depends on \mathbf{U} but does not involve any free parameters to be estimated.² Thus, only \mathbf{M} is multiplied by the parameters Θ . The parameters Θ can be easily determined using a maximum likelihood estimator. Meanwhile, the noise coefficients σ are computed based on the residual. See [22] for the technical details. Notably, the entire parameter estimation can be solved via closed analytic formulae, making the procedure efficient and accurate. Finally, constraints to the parameter values are often included in the parameter estimation procedure. In many ROMs, the quadratic nonlinear terms are assumed to be energy conserved. This is motivated by many geophysical systems where the quadratic nonlinearity is the advection and is a natural conservation quantity. The energy-conserving quadratic nonlinearity in the ROMs prevents the finite time blowup of the solution in the derived model and is physically consistent [38, 59]. Remarkably, closed analytic formulae are still available for parameter estimation in the presence of such constraints; see, e.g., [28, Section 2.5]. With the causation-based ROM framework outlined above, we now turn to a concrete application to illustrate its efficiency in identifying effective parsimonious ROMs for the Kuramoto-Sivashinsky equation.

3 Reduced-Order Models for the Kuramoto-Sivashinsky Equation based on Causal Inference

3.1 Preliminaries and background

The Kuramoto-Sivashinsky equation (KSE) [50, 77] is a fourth-order dissipative partial differential equation (PDE) that can exhibit intricate spatiotemporal chaotic patterns. It is a prototypical model for long-wave instabilities, which has been derived in various contexts of extended non-equilibrium systems that include unstable drift waves in plasmas [53], laminar flame fronts [77], pattern formation in reaction-diffusion systems [50], and long wave fluctuations in thin film [7, 78]. Due to its

¹Typically, for the system (6) to be estimated, the dimension of the noise, d , is the same as the dimension of the state variable n . However, in rare situations when the residual $\frac{d\mathbf{U}}{dt} - \Phi(\mathbf{U})$ computed from the training data associated with an estimated $\Phi(\mathbf{U})$ has a degenerate covariance matrix, the dimension of \mathbf{W} would be lower than n .

²Note that when we seek a purely data-driven ROM, \mathbf{Q} is usually absent in (7). However, the inclusion of such a non-parametric part may be relevant if one has precise prior knowledge about a portion of the vector field.

rich dynamical features, the KSE has served as a test ground for various model reduction methods as well as data assimilation techniques in recent years; see, e.g., [3, 17, 44, 54, 56, 57, 64, 81].

We consider the one-dimensional KSE:

$$\partial_t u = -\nu u_{xxxx} - D u_{xx} - \gamma u u_x, \quad (8)$$

which is posed on a bounded interval, $\mathcal{D} = (0, L)$, and subject to periodic boundary conditions. In (8), ν , D and γ are positive parameters.

Under the given boundary conditions, since the spatial average is a conserved quantity for the solution $u(x, t)$ of Eq. (8), for simplicity, we restrict to initial data with mean zero by imposing

$$\int_0^L u(x, t) dx = 0, \quad \forall t \geq 0. \quad (9)$$

To build up understanding, throughout the numerical experiments reported below, we will also utilize Galerkin truncations of Eq. (8) constructed using either the eigenbasis of the linear operator in (8) or an empirically constructed basis built from the proper orthogonal decomposition.

3.1.1 Galerkin projections of the KSE under the Fourier basis

Due to the assumed periodic boundary conditions, the eigenfunctions of the linear operator $\mathcal{A} = -\nu \partial_{xxxx} - D \partial_{xx}$ in Eq. (8) consist of sine and cosine functions. Thus, the eigenbasis coincides with the Fourier basis. The corresponding Galerkin approximations of Eq. (8) can be determined analytically as given below.

First note that the eigenvalues of the linear operator A subject to the periodic boundary conditions and the additional mean-zero condition (9) are given by

$$\beta_n = -\frac{16\nu\pi^4 n^4}{L^4} + \frac{4D\pi^2 n^2}{L^2}, \quad n \in \mathbb{N}, \quad (10)$$

where \mathbb{N} denotes the set of all positive integers. Each eigenvalue is associated with two eigenfunctions (labeled by a superscript ℓ):

$$e_n^\ell(x) = \begin{cases} \sqrt{\frac{2}{L}} \cos\left(\frac{2\pi n x}{L}\right), & \text{if } \ell = 0, \\ \sqrt{\frac{2}{L}} \sin\left(\frac{2\pi n x}{L}\right), & \text{if } \ell = 1. \end{cases} \quad (11)$$

These eigenfunctions are normalized so that their $L^2(\mathcal{D})$ -norm equal to 1.

Since the eigenfunctions occur in a sine and cosine pair for each wave frequency, we consider Galerkin approximations of Eq. (8) of even dimensions. Denote the $2N$ -dimensional Galerkin approximation of the KSE solution u under the Fourier basis by

$$u_G(x, t) = \sum_{n=1}^N \sum_{\ell=0}^1 y_n^\ell(t) e_n^\ell(x). \quad (12)$$

Then the amplitudes, y_n^ℓ 's, satisfy the following $2N$ -dimensional ODE system

$$\frac{dy_n^\ell}{dt} = \beta_n y_n^\ell + \sum_{p,q=1}^N \sum_{\ell_p, \ell_q=0}^1 \langle B(e_p^{\ell_p}, e_q^{\ell_q}), e_n^\ell \rangle y_p^{\ell_p} y_q^{\ell_q}, \quad 1 \leq n \leq N, \quad \ell \in \{0, 1\}, \quad (13)$$

where $B(u, v) = -\gamma uv_x$ denotes the quadratic nonlinear term in Eq. (8), and $\langle \cdot, \cdot \rangle$ denotes the L^2 -inner product for the underlying Hilbert state space. By direct calculation, we have

$$\langle B(e_p^0, e_q^0), e_n^0 \rangle = \langle B(e_p^0, e_q^1), e_n^1 \rangle = \langle B(e_p^1, e_q^0), e_n^1 \rangle = \langle B(e_p^1, e_q^1), e_n^0 \rangle = 0, \quad \forall p, q, n, \quad (14)$$

$$\langle B(e_p^0, e_q^1), e_n^0 \rangle = \langle B(e_q^1, e_p^0), e_n^0 \rangle = \begin{cases} -\frac{\gamma\pi n}{\sqrt{2}L^{3/2}}, & \text{if } n = p + q, \\ \frac{\gamma\pi(p-q)}{\sqrt{2}L^{3/2}}, & \text{if } n = |p - q|, \\ 0, & \text{otherwise,} \end{cases} \quad (15)$$

and

$$\langle B(e_p^\ell, e_q^\ell), e_n^1 \rangle = \begin{cases} (-1)^\ell \frac{\gamma\pi n}{\sqrt{2}L^{3/2}}, & \text{if } n = p + q, \quad \ell \in \{0, 1\}, \\ \frac{\gamma\pi n}{\sqrt{2}L^{3/2}}, & \text{if } n = |p - q|, \quad \ell \in \{0, 1\}, \\ 0, & \text{otherwise.} \end{cases} \quad (16)$$

Formulas (14)-(16) reveal that most of the nonlinear interaction coefficients $\langle B(e_p^\ell, e_q^\ell), e_n^\ell \rangle$ are zero. The resulting Galerkin system (13) has thus a sparse structure. We will show below in Sec. 3.2 that the causal inference criterion presented in Sec. 2 can be used in a data-driven modeling framework to recover this sparse structure with high fidelity.

3.1.2 Galerkin projections of the KSE under the POD basis

In many applications, empirically computed orthogonal bases can be a more favorable choice than analytic bases due e.g. to their data-adaptive features. We will thus also assess the skill of the causation inference approach when an empirical basis is used instead. Among the most common choices are the proper orthogonal decomposition (POD) [37, 42, 76], and its variants [83]. Of demonstrated relevance for the reduction of nonlinear PDEs are also the principal interaction patterns (PIPs) modes [32, 39, 51, 52] that find a compromise between minimizing tendency error with maximizing explained variance in the resolved modes. In the last decade, related promising techniques such as the dynamic mode decomposition (DMD) [69, 73, 91] have also emerged; see [87] for a discussion on the relationships between PIPs, DMD, and the linear inverse modeling [68].

To fix ideas, we use the POD modes to construct the data-driven Galerkin approximations. Given a cutoff dimension N , we denote the POD basis by $\{\varphi_j : j = 1, \dots, N\}$, where the basis functions are ranked by their energy content. Recall that the basis functions are orthonormal, i.e., $\langle \varphi_j, \varphi_k \rangle = \delta_{jk}$ for all j and k . The corresponding N -dimensional POD-Galerkin system of Eq. (8) reads

$$\frac{dy_n^{\text{POD}}}{dt} = \sum_{j=1}^N A_{nj} y_j^{\text{POD}} + \sum_{i,j=1}^N B_{ij}^n y_i^{\text{POD}} y_j^{\text{POD}}, \quad 1 \leq n \leq N, \quad (17)$$

where

$$A_{nj} = \langle \mathcal{A}\varphi_j, \varphi_n \rangle, \quad B_{ij}^n = \langle B(\varphi_i, \varphi_j), \varphi_n \rangle, \quad (18)$$

with $\mathcal{A} = -\nu\partial_{xxxx} - D\partial_{xx}$ and $B(u, v) = -\gamma uv_x$ as before. Once (17) is solved, the corresponding spatiotemporal field that approximates the KSE solution u can be reconstructed via

$$u_G^{\text{POD}}(x, t) = \sum_{n=1}^N y_n^{\text{POD}}(t) \varphi_n(x). \quad (19)$$

3.1.3 Parameter regime and numerical setup

Throughout Sec. 3, we consider the KSE (8) in the parameter regime given by Table 1, where the true system has $N = 128$ pairs of Fourier modes retained. There are six unstable eigen directions for the chosen regime, and the KSE solution is chaotic with relatively slow decay of correlations.

The KSE is solved by transforming the equation in the Fourier space and by using the exponential time-differencing fourth-order Runge-Kutta (ETDRK4) method proposed in [45] to solve the resulting stiff ODE system. The number of Fourier mode pairs retained (N) and the time step used (Δt) is provided in Table 1.

Table 1: System parameters for the KSE (8)

ν	D	L	γ	Δt	N
8	1	20π	1	0.01	128

It has been checked that a 20-dimension Galerkin system (based either on the eigenbasis or the POD basis) is sufficient to reproduce the dynamical and statistical features in the solution of the KSE for the chosen regime. We will then test 20-dimensional causation-based ROMs with different sparsity percentages in the contexts of both eigenbasis and POD basis. We intentionally choose a parameter regime in which the dimension of a high-fidelity Galerkin approximation is not too large in order to not inflate too much the number of candidate functions in the learning library used for computing the causation entropy; see again Sec. 2.2.3. See also Sec. 4 for some discussions about applying the framework to obtain larger causation-based ROMs with dimensions in the hundreds when needed.

All the Galerkin approximations of the KSE (8), either constructed from the Fourier basis or the POD basis, are solved using the fourth-order Runge-Kutta method. The causation-based ROMs as well as the thresholded POD-Galerkin systems to be introduced later are simulated with their drift parts approximated using the fourth-order Runge-Kutta method and the stochastic terms approximated using the Euler-Maruyama scheme. The system (27) involved in the data assimilation experiment below is simulated using the Euler-Maruyama scheme for simplicity, which turns out to be sufficient since the involvement of observational data helps alleviate the stiffness of its drift part. The time step size Δt for all these models is the same as the one used for solving the PDE itself.

The initial data for the KSE is taken to be $u_0 = \cos(2\pi x/L)$, and the computed solution over the time window $[10^4, 5 \times 10^4]$ is used for learning the POD basis as well as for training the related ROMs used in Sec. 3.3 and Sec. 3.4. To compute the coefficients involved in the POD-Galerkin system (17), we approximate each POD basis function using 64 pairs of Fourier modes and then perform the differentiation and integration involved in (18) analytically. For reasons explained in Sec. 3.2, the causation-based ROMs used in this subsection are trained using the solution for the Fourier-Galerkin systems, still over the time window $[10^4, 5 \times 10^4]$.

3.2 Data-driven inverse models under the Fourier basis

As pointed out in Sec. 3.1.1, the Galerkin approximations of the KSE (8) under the Fourier basis have a sparse structure. Such systems thus provide a good first proof of concept testbed to check

whether the causal inference criterion presented in Sec. 2 can differentiate monomials appearing in the Fourier-Galerkin systems from those that do not when all possible linear and quadratic terms are included in the function library used for model identification.

For this purpose, we place the KSE in the parameter regime given in Sec. 3.1.3 and use the 20-dimensional Fourier-Galerkin system of the form (13) as the true model to generate the training data. We will first examine to what extent causation entropy can identify the constituent terms in the Galerkin model from the predefined function library. Once the model terms are selected based on a given cutoff threshold of the causation entropy value, we perform a subsequent parameter estimation procedure to identify the causation-based ROM and check its performance. As mentioned in Sec. 3.1.3, the chosen dimension of the Galerkin approximation, 20, is made such that the KSE solution dynamics are well captured by the Galerkin system.

In the numerical experiment, we include all possible linear and quadratic monomials in the function library. There are thus a total of 230 candidate functions for the chosen Galerkin dimension, consisting of 20 linear terms and 210 quadratic terms. We adopt the following ordering to arrange the 230 library functions. Denoting the 20 unknowns y_n^ℓ ($\ell = 0, 1, n = 1, \dots, 10$) of the Galerkin system by $\mathbf{Y} = (y_1^0, \dots, y_{10}^0, y_1^1, \dots, y_{10}^1)^\top$ for convenience, the library functions \mathbf{f} are arranged in the order of

$$\{Y_1, \dots, Y_{20}\} \quad \text{followed by} \quad \{Y_j Y_k \mid 1 \leq j \leq k \leq 20\}, \quad (20)$$

where the following lexicographic order for (j, k) is adopted for the quadratic terms: $(j_1, k_1) < (j_2, k_2)$ if $(j_1 < j_2)$ or $j_1 = j_2$ and $k_1 < k_2$.

Following the description in Sec. 2.2.3, we compute the causation entropy from each library function f_m to the i th equation, $C_{f_m \rightarrow \dot{Y}_i | [\mathbf{f} \setminus f_m]}$, according to the approximation formula (5). In total, there are $230 \times 20 = 4600$ causation entropy values to compute. These values are shown in Fig. 1, which are grouped by equation, with the first 230 values (from left) for the first equation and the next 230 values for the second equation, etc. There is a visible gap in Fig. 1 that separates large causation entropy values (such as those above the red dashed horizontal line) from the smaller ones (below the blue dashed horizontal line), with only very few exceptions falling in between. One is then tempted to suspect that the cutoff threshold for the causation entropy value should fall within this gap.

In the remainder of this section, we use the more severe cutoff threshold identified by the red dashed line in Fig. 1 as the cutoff threshold, which corresponds to a numerical value of 0.65 in contrast to 0.05 for the blue dashed line. There are 283 terms whose causation entropy values are above this threshold of 0.65. It turns out all these 283 identified terms are present in the true model, which itself has 295 terms. Figure 2 (panel B) shows the distribution of the identified 283 terms, while that for the true 20-dimensional Galerkin model (13) is shown in panel A of this figure. The 12 terms in the true model not identified with this cutoff threshold are shown in panel C of Fig. 2.

As can be seen in Fig. 2, the causation entropy criterion is remarkably successful in identifying the true sparse model. In particular, it has a negligible mismatch rate of $12/4600 = 0.26\%$ for the total 4600 possible terms to be sifted through. It turns out that all these 12 mismatch terms are quadratic terms, while all the linear terms of the model are correctly identified. Indeed, the linear part of the true model is a diagonal matrix with eigenvalues on the diagonal (see Eq. (13)), which is represented by the left-most diagonal block in panel A of Fig. 2 and is captured in full with the chosen cutoff threshold as shown in panel B of this figure.

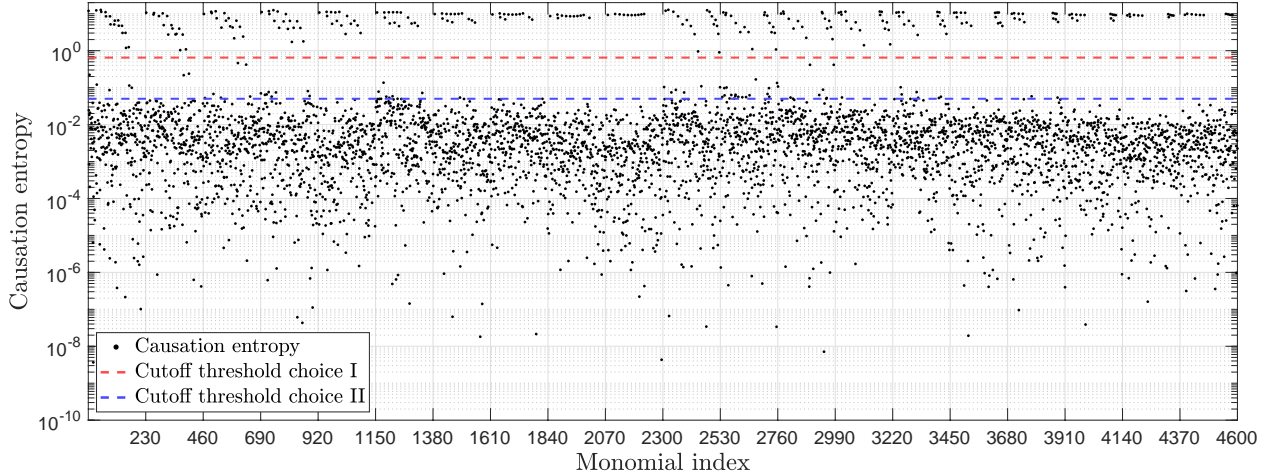


Figure 1: Causation entropy that ranks the importance of the library functions for learning a data-driven quadratic inverse model of the 20-dimensional Fourier Galerkin system of the form (13). The candidate function library \mathbf{f} includes all of the 230 linear and quadratic monomials constructed from the 20 components of the unknown \mathbf{Y} as listed in (20). The causation entropy from each library function f_m to the i th equation, $C_{f_m \rightarrow Y_i}[[\mathbf{f} \setminus f_m]]$, is computed according to the approximation formula (5) given in Sec. 2.2.3. The parameter regime is the one given in Sec. 3.1.3. The causation entropy values are grouped by equation, with the first 230 values (from left) for the first equation, and the next 230 values for the second equation, etc. Also shown are two cutoff thresholds, 0.65 (red line) and 0.05 (blue line). It has been checked that the causation entropy values for all the terms appearing in the true Galerkin system are above the blue line, confirming thus the relevance of this casual inference criterion in identifying constituent terms in the data-driven model.

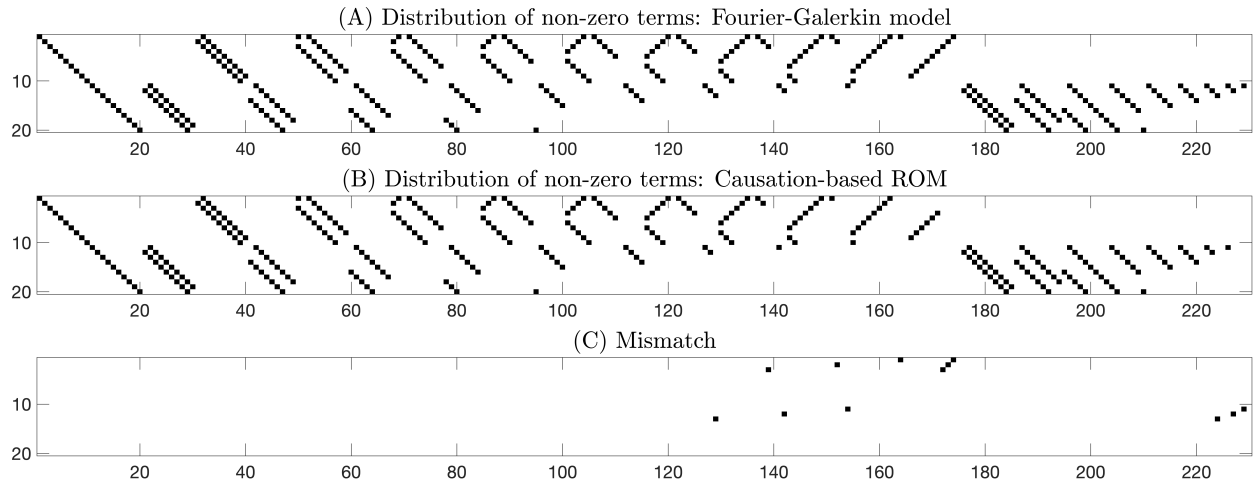


Figure 2: Visualization of the distribution of the constituent terms in the 230 function library for the true Galerkin model (panel A) and the learned model (panel B). The learned model is constructed with the cutoff threshold for the causation entropy taken to be 0.65 (red line in Fig. 1). In each panel, the vertical axis consists of 20 rows with each row corresponding to one equation, and the horizontal axis consists of 230 columns with each column corresponding to one function in the learning library. They form thus a 20×230 mesh. A black square in the (i, j) -th grid indicates the j th monomial in the library is present in the i th equation. The functions in the library are ordered in the way given by (20). In particular, the linear terms are placed before the quadratic terms. For instance, the left-most diagonal block in panel A shows that the linear part of the true Galerkin model is diagonal. The mismatches between the learned model and the true model are shown in panel C. There are 12 mismatched terms, all of which are quadratic terms. It has been checked that all these 12 terms are present in the true model, but are missing in the learned model.

Once the constituent terms are identified, we use a standard maximum likelihood estimator to determine the model coefficients; see Sec. 2.2.4. For this purpose, we use the same training solution data used in the previous causal inference step. Among the 283 coefficients, 20 coefficients on the diagonal of the matrix are to be learned for the linear part, and the remaining 263 coefficients are for the nonlinear terms. The numerical values of these coefficients are graphically shown in Fig. 3. For the linear part (top panels of Fig. 3), the learned model coefficients recover these for the true model with high precision. We have checked that the relative error is below 0.06% for all the 20 coefficients. For the nonlinear terms (bottom panels of Fig. 3), the largest differences between the learned model coefficients and the true ones occur at the 12 mismatched terms, as expected. Outside of these mismatched terms, the error is one-order smaller (on the scale of 10^{-3}) compared with those shown in panel F of Fig. 3. Note also that the causation entropy for the mismatched terms all fall below the red dashed line in Fig. 1 and thus being filtered out in the learned model for this chosen cutoff threshold. We then expect that they play a less important role than the other 283 terms in “orchestrating” the dynamics in the true model. Once the drift terms and their coefficients are determined, the training residual is fitted with a Gaussian noise term (see $\sigma \dot{W}(t)$ in (6)). The noise amplitude matrix σ comes with very small entries on the scale of 10^{-7} . Thus, the noise term is essentially negligible in the resulting causation-based ROMs. It turns out that the learned model with this cutoff threshold can already capture faithfully the true dynamics as shown in Figs. 4 and 5.

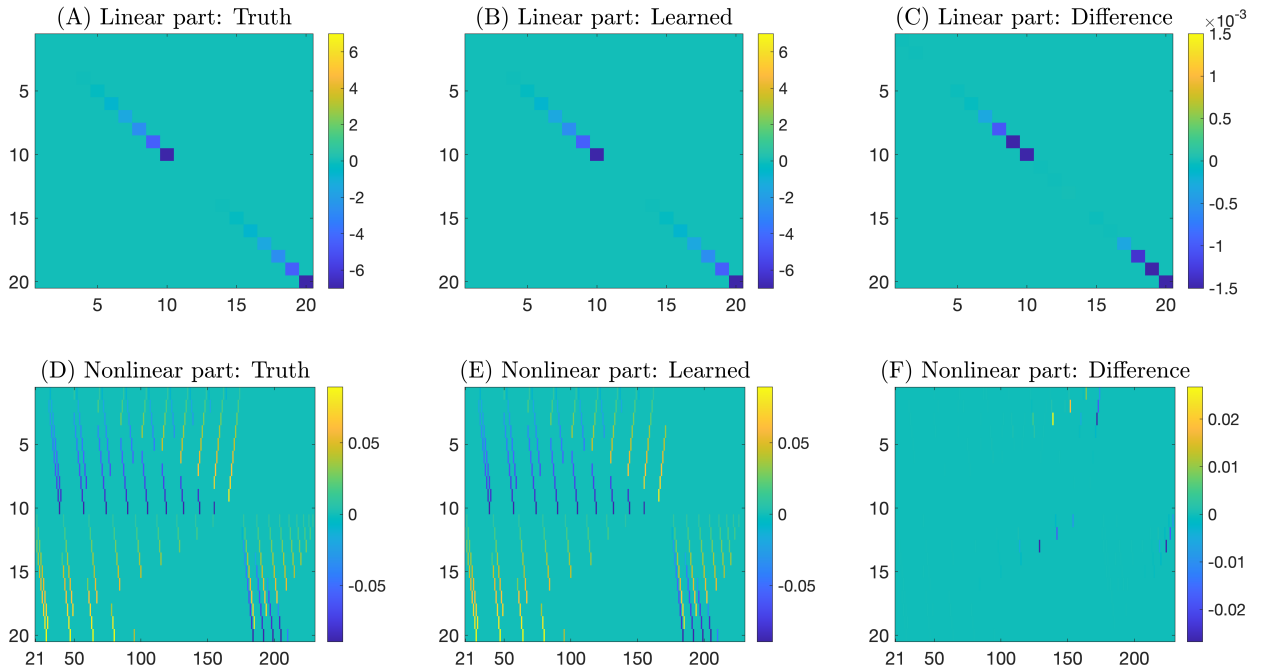


Figure 3: Visualization of the model coefficients for the 20-dimensional Fourier-Galerkin system (true model) and the causation-based ROM (learned model). For the true model, all non-zero coefficients occur for the terms marked by black squares shown in panel A of Fig. 2. We separated the linear terms (panel A here) with the nonlinear terms (panel D here) for a better visualization, since the coefficients for some of the linear terms are two-order larger than those for the nonlinear terms. The sparsity structure for the learned model is the one shown in panel B of Fig. 2.

In particular, we show in Fig. 4 the reconstructed spatiotemporal field for the true Galerkin model defined by (12) (left panel) and its analog from the causation-based ROM (right panel).

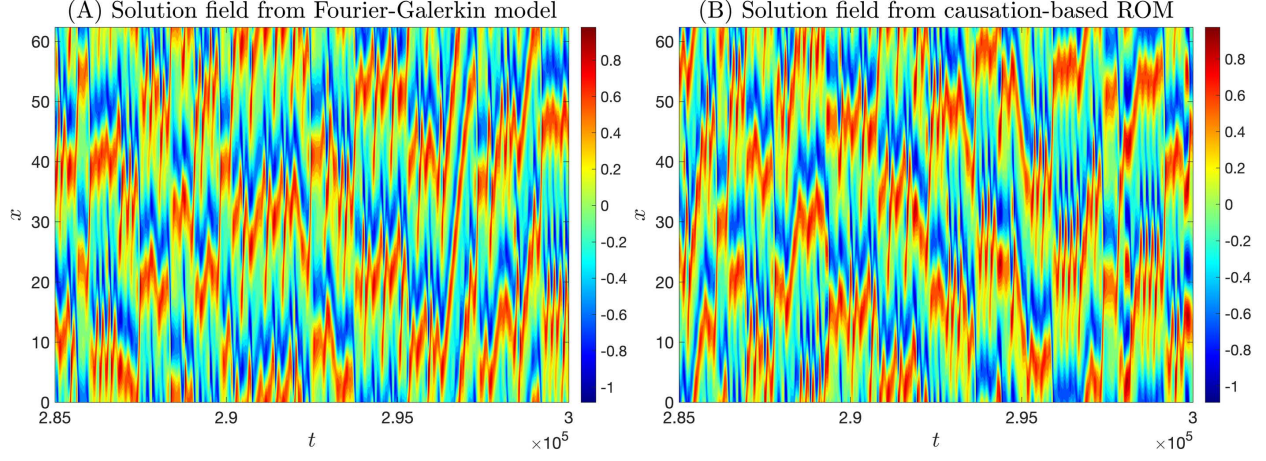


Figure 4: Comparison of the reconstructed solution fields obtained using (12) for the 20-dimensional Fourier-Galerkin system (13) (left panel) and for the causation-based ROM of the same dimension (right panel). The results are shown here in a time window well beyond the training window $[10^4, 5 \times 10^4]$.

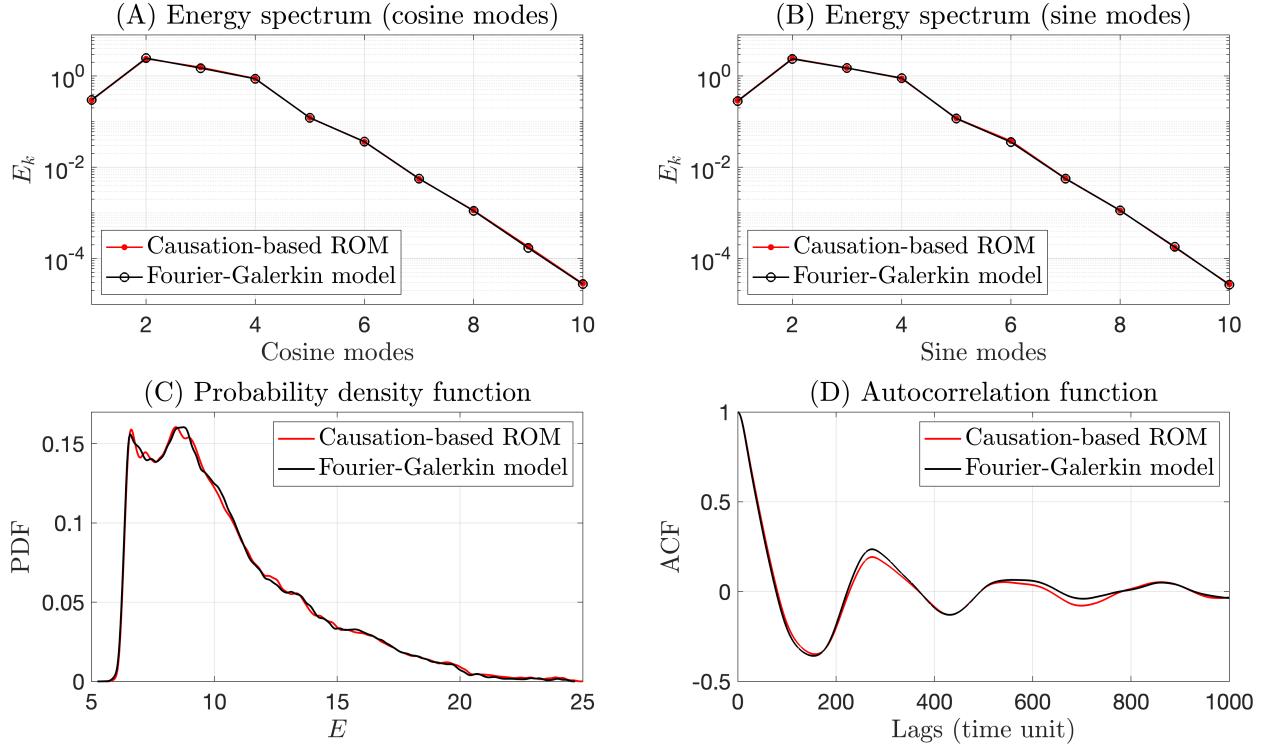


Figure 5: Comparison of statistics between the 20-dimensional Fourier-Galerkin system and the associated causation-based ROM. The energy spectrum E_k shown here is computed outside of the training window by averaging $(y_k^\ell(t))^2$ over the time window $[5 \times 10^4, 3 \times 10^5]$, for all the components $k = 1, \dots, 10$ and $\ell = 0, 1$. The cosine modes correspond to $\ell = 0$ (Panel A) and sine modes correspond to $\ell = 1$ (Panel B). The PDFs and the ACFs (shown in the bottom panels) for the kinetic energy $E(t) = \sum_{k=1}^{10} \sum_{\ell=0}^1 (y_k^\ell(t))^2$ are computed over the same time window $[5 \times 10^4, 3 \times 10^5]$. We also note that the energy spectra for the sine and cosine modes corresponding to the same frequency k are essentially the same for the Galerkin model (as well as for the learned model), indicating a type of equipartition of energy occurring in the model.

The solutions are shown in a time window that is far beyond the training window $[10^4, 5 \times 10^4]$. The chaotic dynamics from the learned model are essentially indistinguishable from those in the true model, with local maxima (reddish patches) and local minima (bluish patches) progressing in a zigzag way as time evolves, forming a rich variety of local patterns. In that respect, we also point out that the long thin reddish strip observed in the left panel formed in the time window $[2.96 \times 10^5, 2.97 \times 10^5]$, which propagates from the left side of the domain ($x = 0$) all the way up to almost the right side of the domain, has also been observed in other time windows for the learned model. This good reproduction of the dynamics is further confirmed at the statistical level as shown in Fig. 5 for the energy spectrum E_k (top panels) as well as the probability density function (PDF) and the autocorrelation function (ACF) of the kinetic energy E (bottom panels); see the caption of this figure for further details.

Going back to Fig. 1, when the more conservative cutoff threshold 0.05 (corresponding to the blue dashed line) is used, the corresponding causation-based ROM contains a total of 354 terms, which includes all of the 295 terms appearing in the true Galerkin model. The performance of this new causation-based ROM is similar to those shown in Fig. 4B and Fig. 5. This indicates that the terms whose causation entropy values fall in between the gap marked by the red and blue dashed lines in Fig. 1 already play very little role in determining the dynamics of the learned model.

We also note that the existence of a clear gap to separate the larger and smaller causation entropy values, such as shown in Fig. 1 seems to be tied to the fact that the Fourier-Galerkin systems (13) themselves admit a sparse structure; see again (14)–(16). When other (global) basis functions are used, the corresponding Galerkin system may no longer be sparse. As such, one should no longer expect a clear gap to present in the causation entropy plot. However, as shown below using the POD basis, the ranking of the library terms provided by the causation entropy still offers a compelling way to obtain skillful yet significantly sparsified models.

3.3 Data-driven inverse models under the POD basis

We turn now to examine the situation when the underlying orthogonal basis is constructed empirically instead, which is taken to be the POD basis here. For benchmarking purposes, we will compare the performance of the learned model with that of the POD-Galerkin system (17) as well as a thresholded version of the Galerkin system obtained by removing terms whose coefficients in absolute value are below a given threshold to achieve a specified sparsity percentage.

The causation entropy, as computed using the 20-dimensional POD projection of the KSE solution, is shown in Fig. 6. Unlike the case with the Fourier basis shown in Fig. 1, we no longer see a gap that separates a small fraction of larger causation entropy values with the remaining smaller causation entropy values. As mentioned at the end of the previous subsection, a plausible reason is that the POD-Galerkin system (17) itself does not have a sparse structure. Recall that the 20-dimensional Fourier-Galerkin system (13) utilized in the previous subsection has only 295 terms in its vector field, accounting for about 6.41% of the total $20 \times 230 = 4600$ possible monomials in a 20-dimensional quadratic vector field (excluding constant terms). In sharp contrast, almost all the 4600 terms are present in the 20-dimensional POD-Galerkin system (17). As shown in Fig. 7, the absolute value of the coefficients falls in the range $[10^{-5}, 10^{-1}]$ for 96.5% of the terms (namely 4439 terms) in this POD-Galerkin system.

Due to the lack of any obvious cutoff thresholds appearing in the distribution of the causation entropy values, a possible way to proceed is to construct a hierarchy of inverse models that main-

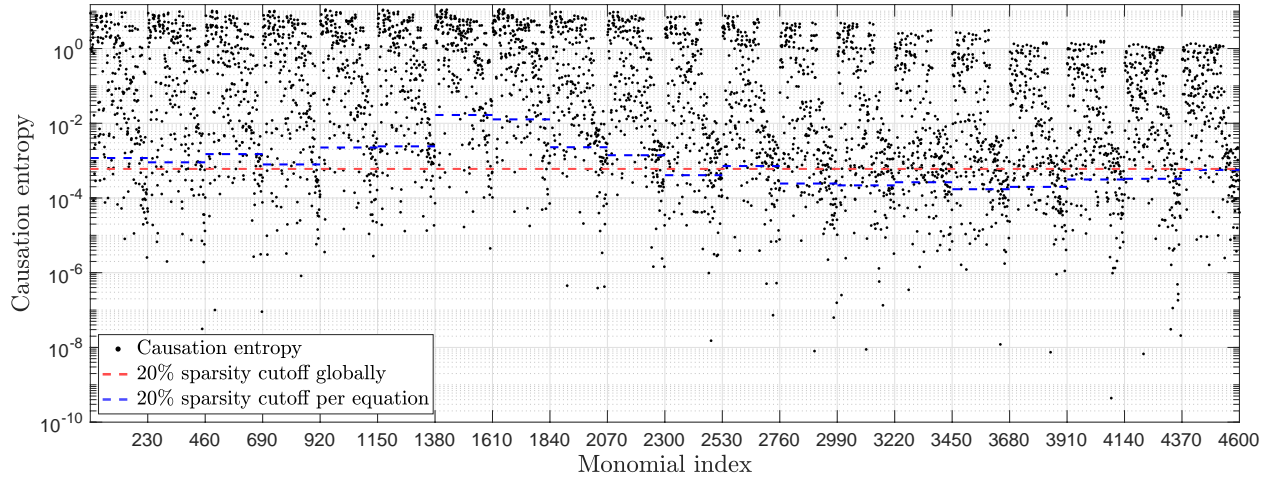


Figure 6: Causation entropy that ranks the library functions for learning a data-driven quadratic inverse model of the 20-dimensional POD Galerkin system (17). The causation entropy values are grouped by equation in the same way as done in Fig. 1. Also shown are the cutoff thresholds for ensuring 20% sparsity based on two strategies: the red dashed line corresponds to the threshold 6×10^{-4} that separates the lower 20% of all the 4600 causation entropy values from the remaining 80%, while the blue dashed line segments correspond to the thresholds that separate the lower 20% of the 230 causation entropy values for each of the 20 equations. The total number of terms kept in the learned models based on these two strategies are the same, but the constituent terms kept in the corresponding identified models are slightly different.

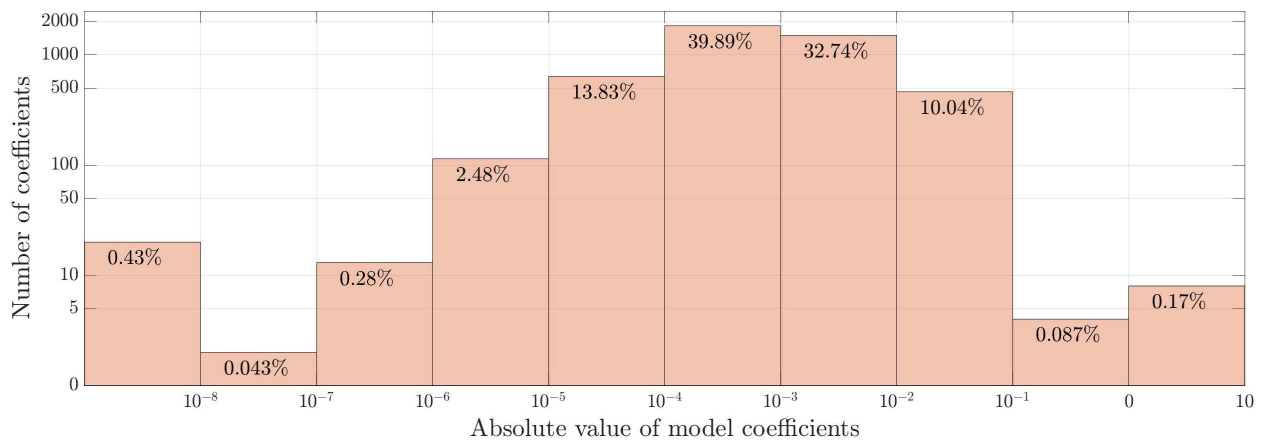


Figure 7: Distribution of the model coefficients for all the 4600 terms in the 20-dimensional POD-Galerkin system (17) of the KSE (8), for the parameter regime given by Sec. 3.1.3.

tain different sparsity percentages by adjusting the cutoff threshold. There are two different ways to carry out this cutoff procedure. One way is to choose a uniform cutoff threshold for all the equations, such as indicated by the red dashed line in Fig. 6. Apparently, this approach only ensures that a given percentage of terms is removed from the learned model but does not guarantee that the percentage of terms removed is the same for each equation in the system. The other way is to choose a custom cutoff threshold for each equation, such as indicated by the blue dashed lines in Fig. 6 to achieve the same sparsity percentage for each equation. In principle, the two cutoff procedures can lead to quite different reduced models, especially when the range of the causation entropy values varies significantly from equation to equation. However, for the model considered here, it has been checked that the ROMs obtained by the two approaches for a given sparsity percentage lead to similar modeling performance. For all the numerical results reported below, the causation-based ROMs are constructed using the latter approach to gain the same sparsity percentage for all the equations. Once the constituent terms are determined based on a chosen cutoff threshold strategy for the causation entropy values, we use again the maximum likelihood estimator to determine the model coefficients in the causation-based ROMs; see Sec. 2.2.4.

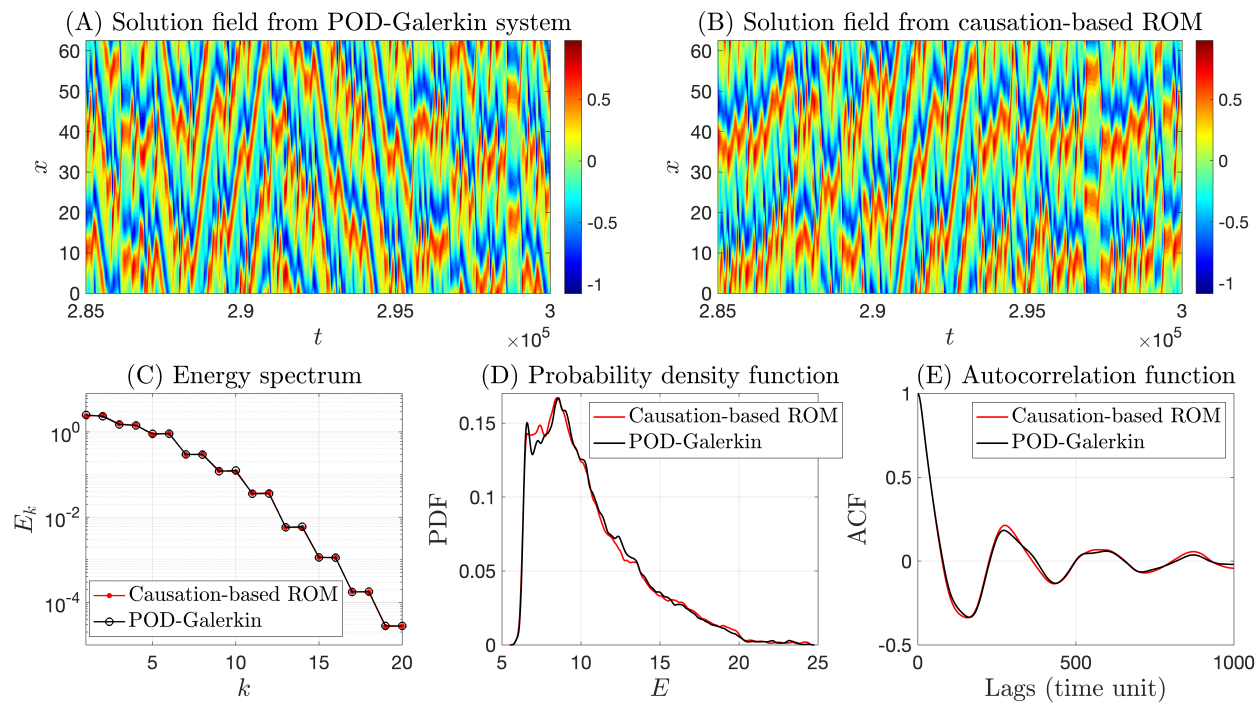


Figure 8: Performance of the 20-dimensional causation-based ROM under POD basis, with a 20% sparsity cutoff per equation, in comparison with the 20-dimensional POD-Galerkin system. The reconstructed solution fields are shown in Panel A for the POD-Galerkin system and Panel B for the learned model. The energy spectrum E_k is shown in Panel C. The PDFs and the ACFs of the kinetic energy E are shown in Panels D and E, respectively. The energy spectra E_k 's and the kinetic energy E are computed in the same way as described in the caption of Fig. 5. Like in Fig. 5, the time window used for computing E_k and E is $[5 \times 10^4, 3 \times 10^5]$, which is outside of the training window $[10^4, 5 \times 10^4]$.

In Fig. 8, we present the skill of the 20-dimensional causation-based ROM with a 20% sparsity. As can be observed, even though the ROM contains 20% fewer terms than the corresponding POD-Galerkin system, it can faithfully reproduce the essential dynamical features and the associated

statistics appearing in the solution of the POD-Galerkin system. We also checked that even by increasing the sparsity percentage to 50%, the causation-based ROM can still produce chaotic transient dynamics over a long time window with the corresponding solution field resembling that shown in Panels A and B of Fig. 8, although the solution eventually becomes periodic after about 3.6×10^6 time-step iterations. This slow drift to periodic dynamics after long-time integration observed for “severely” truncated causation-based ROMs is not a surprise. The KSE is known to have many periodic dynamics regimes interlaced with chaotic dynamics regimes [43]. In other words, the chaotic attractors observed for the KSE may be prone to instability under perturbations depending on the parameter regimes considered. Since a ROM can be viewed as a perturbation of the original KSE model, it is possible for the dynamics of a highly truncated ROM to be (gradually) pushed towards the basin of attraction of a periodic attractor in a nearby regime.

Although the dynamical features of the KSE dictates that one may not be able to use a too sparse ROM to capture long-term statistics for certain parameter regimes, the fact that such a causation-based ROM can still reproduce accurately short-time features suggest its potential usage for other purposes such as data assimilation and short-term trajectory prediction. In the next subsection, we demonstrate the advantage of such highly sparse causation-based ROMs in the context of data assimilation with partial observations.

3.4 Application to data assimilation with partial observations

We now illustrate the performance of causation-based ROMs in the context of data assimilation to recover unobserved higher-frequency mode dynamics based on observation data for a few low-frequency mode dynamics. As a benchmark, we also compare the results obtained from a thresholded stochastic POD-Galerkin model described below. For simplicity, we assume that the observation data is available continuously in time, and we perform the data assimilation with the ensemble Kalman-Bucy filter (EnKBF) [4, 6] for both reduced systems.

The thresholded Galerkin system is obtained from the true 20-dimensional POD-Galerkin system as follows. We rank the coefficients of the true Galerkin system from large to small in absolute value and then drop the terms with coefficients below a cutoff value that is determined to ensure the number of monomials retained is the same as that of the employed causation-based ROM. After identifying the terms to be kept, we use the maximum likelihood method to estimate its model coefficients. The residual from this parameter estimation process is then used to determine the covariance matrix of the additive noise term in the final thresholded Galerkin model.

For the sake of clarity, we first provide below some details about the EnKBF applied to a generic n -dimensional SDE system of the form (6):

$$\frac{d\mathbf{U}}{dt} = \Phi(\mathbf{U}) + \sigma \dot{\mathbf{W}}(t), \quad (21)$$

in which the noise amplitude matrix σ is assumed to be $n \times n$ -dimensional and the first r component of \mathbf{U} is taken to be observed while the remaining components to be unobserved. We denote

$$\begin{aligned} \mathbf{y} &= (U_1, \dots, U_r)^T, & \mathbf{z} &= (U_{r+1}, \dots, U_n)^T, \\ \mathbf{W}_1 &= (W_1, \dots, W_r)^T, & \mathbf{W}_2 &= (W_{r+1}, \dots, W_n)^T. \end{aligned} \quad (22)$$

We also decompose σ into four submatrices

$$\sigma = \begin{pmatrix} \sigma_{11} & \sigma_{12} \\ \sigma_{21} & \sigma_{22} \end{pmatrix}, \quad (23)$$

where the dimensions of σ_{11} and σ_{22} are $r \times r$ and $(n-r) \times (n-r)$, respectively. We then rewrite (21) using (\mathbf{y}, \mathbf{z}) as follows

$$\begin{aligned} \frac{d\mathbf{y}}{dt} &= \mathbf{g}_1(\mathbf{y}, \mathbf{z}) + \sigma_{11} \dot{\mathbf{W}}_1(t), \\ \frac{d\mathbf{z}}{dt} &= \mathbf{g}_2(\mathbf{y}, \mathbf{z}) + \sigma_{22} \dot{\mathbf{W}}_2(t), \end{aligned} \quad (24)$$

where \mathbf{g}_1 and \mathbf{g}_2 denote respectively the first r and the remaining $n-r$ components of the (nonlinear) function Φ in (21). Note also that compared with the original system (21), we decoupled the noise terms in the \mathbf{y} - and \mathbf{z} -subsystems by dropping $\sigma_{12} \dot{\mathbf{W}}_2(t)$ in the \mathbf{y} -subsystem and $\sigma_{21} \dot{\mathbf{W}}_1(t)$ in the \mathbf{z} -subsystem for simplicity. In practice, the noise amplitude matrix σ is oftentimes diagonal dominant. This is, in particular, true for the KSE problem considered here. Additionally, the noise in both the causation-based ROM and the thresholded POD-Galerkin system is very weak. Thus, such an approximation has little impact on the accuracy of final data assimilation results.

Assume that a total of p ensemble members are used in the EnKBF. Denote the collection of all the p ensemble members at time t by

$$\mathbf{Z}(t) = (\mathbf{z}_1(t), \mathbf{z}_2(t), \dots, \mathbf{z}_p(t))^T.$$

Denote also the observation data of \mathbf{y} at time t by $\mathbf{y}_{\text{obs}}(t)$. We define then

$$\bar{\mathbf{Z}}(t) = \frac{1}{p} \sum_{\ell=1}^p \mathbf{z}_\ell(t), \quad \bar{\mathbf{g}}_2(\mathbf{y}_{\text{obs}}(t), \mathbf{Z}(t)) = \frac{1}{p} \sum_{\ell=1}^p \mathbf{g}_2(\mathbf{y}_{\text{obs}}(t), \mathbf{z}_\ell(t)), \quad (25)$$

and

$$\mathcal{N}(\mathbf{y}_{\text{obs}}(t), \mathbf{Z}(t)) = \frac{1}{(p-1)} \sum_{\ell=1}^p (\mathbf{z}_\ell(t) - \bar{\mathbf{Z}}(t)) \left(\mathbf{g}_2(\mathbf{y}_{\text{obs}}(t), \mathbf{z}_\ell(t)) - \bar{\mathbf{g}}_2(\mathbf{y}_{\text{obs}}(t), \mathbf{Z}(t)) \right)^T C^{-1}, \quad (26)$$

where $C = \sigma_{22} \sigma_{22}^T$.

Then, each ensemble member \mathbf{z}_i , $i = 1, 2, \dots, p$, of the EnKBF is computed using

$$\begin{aligned} \frac{d\mathbf{z}_i}{dt} &= \mathbf{g}_2(\mathbf{y}_{\text{obs}}(t), \mathbf{z}_i) + \sigma_{22} \dot{\mathbf{W}}_{2,i}(t) \\ &\quad - \mathcal{N}(\mathbf{y}_{\text{obs}}(t), \mathbf{Z}(t)) \left[\mathbf{g}_1(\mathbf{y}_{\text{obs}}(t), \mathbf{z}_i) - \dot{\mathbf{y}}_{\text{obs}}(t) + \sigma_{11} \dot{\mathbf{W}}_{1,i}(t) \right], \end{aligned} \quad (27)$$

where $\mathbf{W}_{1,i}$ and $\mathbf{W}_{2,i}$ are respectively r -dimensional and $(n-r)$ -dimensional Brownian motions for $i = 1, 2, \dots, p$, with their components to be all mutually independent.

The setup of the data assimilation experiment is as follows. We observe the amplitudes of the first three POD modes of the KSE solutions and aim to recover the amplitudes of the few dominant unobserved modes by applying the EnKBF to either the 20-dimensional causation-based

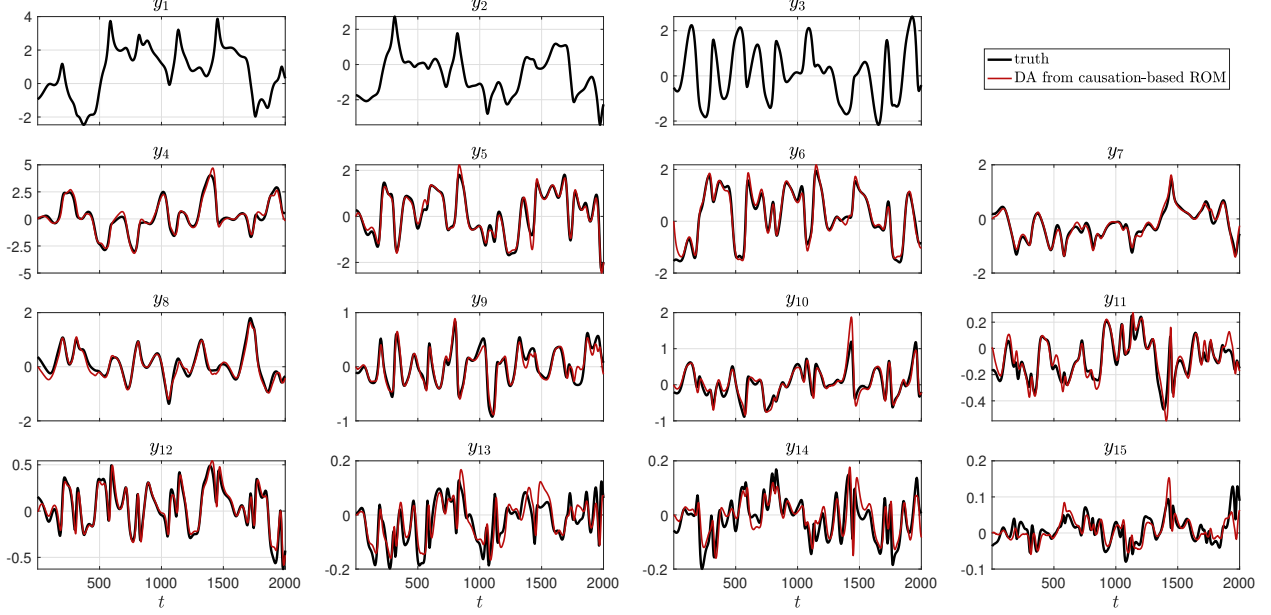


Figure 9: The black curves show the projections of the true KSE solution onto the first 15 POD modes, with the first three components y_1 , y_2 , and y_3 taken to be the observed modes in the data assimilation experiments. The red curves show the assimilated ensemble mean dynamics of the unobserved POD modes from the 20-dimensional causation-based ROM, with 90% sparsity.

ROM with a large sparsity percentage or the corresponding 20-dimensional thresholded POD-Galerkin system with the same sparsity percentage. We take the size of the EnKBF ensemble to be $p = 500$, and the unobserved variables are initialized to be zero for all the ensemble simulations. The sparsity percentage of the ROMs is taken to be 90%, resulting in 460 terms in the drift part of both the causation-based ROM and the thresholded POD-Galerkin system. The KSE is simulated over the time window $[0, 2000]$ with the initial data taken to be the solution profile at the last time instant of the training data utilized for constructing the POD basis function as well as the training of the ROMs.

In the first row of Fig. 9, we show the time series of the three observed POD modes. On average, these three modes capture about 63.5% of the kinetic energy in the KSE solution for the considered parameter regime, while above 99% of the kinetic energy is captured by the first 10 POD modes. As shown in Fig. 9 (black curves), modes 4 to 10 still have quite large amplitude oscillations almost comparable with those of the first three modes, and they evolve on different time scales. The fact that the unobserved dynamics still contain, on average, nearly 40% of the kinetic energy and that their projected dynamics reveal multi-scale, highly chaotic oscillatory features present arguably a challenging test ground for the data assimilation experiment.

The red curves in Fig. 9 represent the posterior mean of the unobserved modes y_4 through y_{15} (red curves) obtained from the EnKBF applied to the causation-based ROM, in comparison with the corresponding true POD projections of the KSE solutions (black curves). Despite its highly sparse nature, with 90% sparsity compared with the true POD-Galerkin system of the same dimension, the causation-based ROM is able to recover with high fidelity all the energetic unobserved modes, y_4, \dots, y_{12} . The skill for the remaining small amplitude modes, y_{13}, \dots, y_{20} , deteriorates as the mode index increases, as can be seen in Fig. 9 for modes y_{13} , y_{14} , and y_{15} . However, these 8 modes

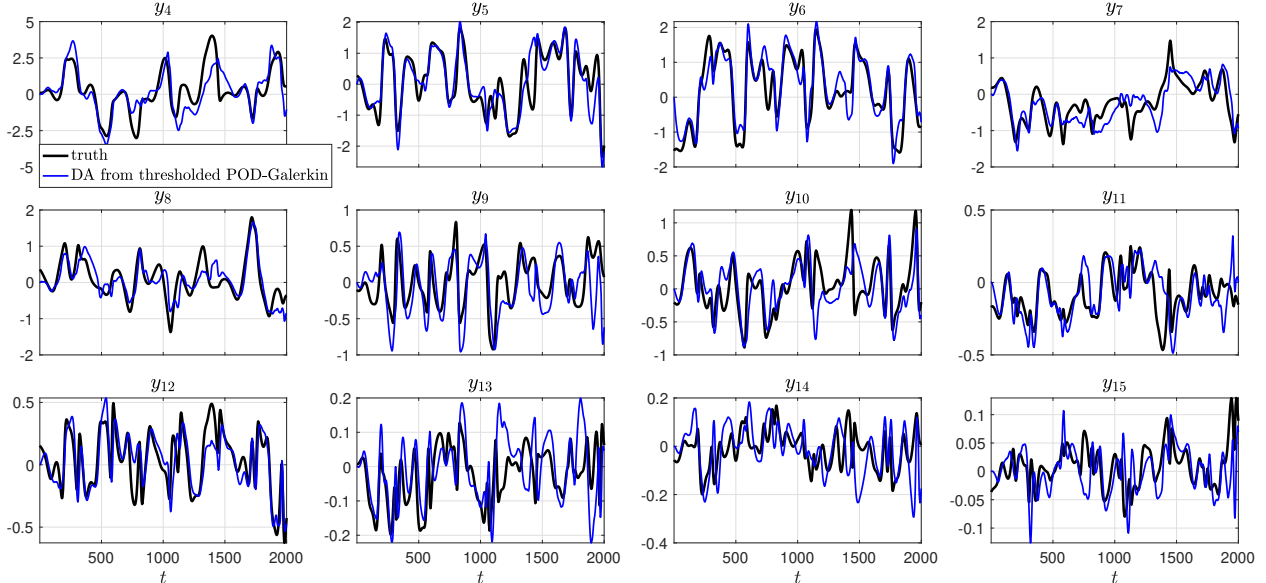


Figure 10: The assimilated ensemble mean dynamics of the unobserved POD modes from the EnKBF of the 20-dimensional thresholded POD-Galerkin system with 90% sparsity (blue curve), in comparison with the POD projections of the true KSE solution (black curves).

contain, on average, only approximately 0.13% of the solution energy.

As a comparison, the corresponding results for the 20-dimensional thresholded POD-Galerkin system with 90% sparsity are shown in Fig. 10. The skill is much less good than that obtained from the causation-based ROM. When comparing these unobserved dynamics at the spatiotemporal field level, it also reveals that the thresholded POD-Galerkin system with this high truncation ratio suffers particularly severely when there is a relatively abrupt change in the solution dynamics, such as shown at around $t = 1450$ in Fig. 11. Finally, we mention that the time series for all the 500 ensemble members in the data assimilation essentially coincide with each other for both of the two ROMs analyzed due to the fact that the involved noise amplitude matrix σ for both ROMs employed has entries all close to zero.

The above results show that causation entropy can indeed be utilized to rank the relative importance of candidate terms from a given function library for the construction of skillful sparse inverse models. The obtained superior data assimilation skills compared with those from the thresholded POD-Galerkin system also illustrate that a naive truncation based on the numerical values of the model coefficients in e.g. a POD-Galerkin system may not be appropriate, especially when a highly truncated ROM is sought.

4 Discussion and Conclusions

In this article, we analyzed an efficient approach to identifying data-driven ROMs with a sparse structure using a quantitative indicator called causation entropy. For each potential building-block function f in the vector field of the i -th component u_i , the associated causation entropy measures the difference between the entropy of \dot{u}_i conditioned on the whole set of candidate functions and the one conditioned on the set without f ; see (2). Thus, it quantifies statistically the additional

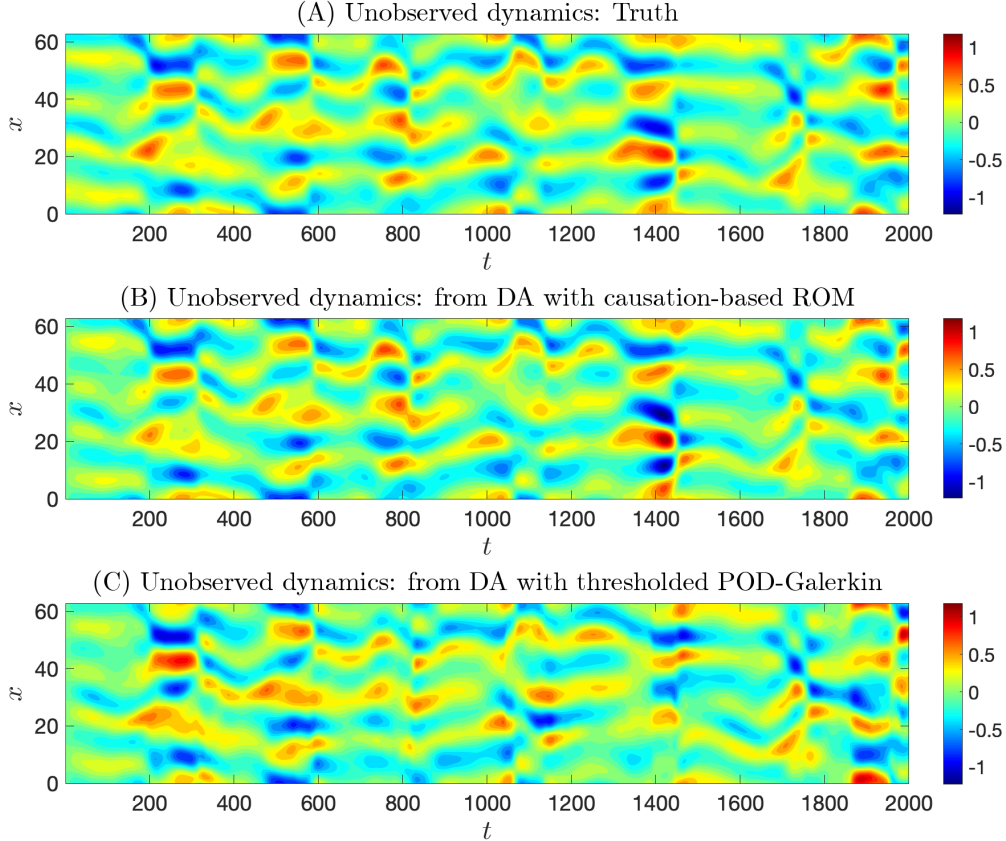


Figure 11: Comparison of the true unobserved spatiotemporal field (top panel) with those reconstructed based on the assimilated ensemble mean dynamics shown in Fig. 9 for the causation-based ROM (middle panel) and in Fig. 10 for the thresholded POD-Galerkin system (bottom panel).

contribution of each term to the underlying dynamics beyond the information already captured by all the other terms in the model ansatz.

The ranking of the candidate terms provided by the causation entropy leads to a hierarchy of parsimonious structures for the ROMs controlled by a cutoff threshold parameter. The model coefficients for the corresponding causation-based ROMs can then be learned using standard parameter estimation techniques, such as the maximum likelihood estimator; cf. Sec. 2.2.4. Illustrating on the Kuramoto-Sivashinky equation, we showed in Sec. 3 that the obtained causation-based ROMs are skillful in both recovering long-term statistics and inferring unobserved dynamics via data assimilation when only a small subset of the ROM’s state variables is observed.

We conclude by outlining some potential future directions to be explored. For this purpose, we want to emphasize first that, when building up the causation-based ROMs, it is straightforward to add additional physically relevant constraints, such as skew symmetry for certain linear terms and energy conservation for the quadratic nonlinearity. For the results shown in Sec. 2.2.4, the obtained ROMs turn out to be stable without enforcing energy conservation constraints, even though the quadratic term in the Kuramoto-Sivashinky equation conserves energy. However, such a constraint is expected to be important, e.g., in the reduction of fluid problems in turbulent regimes. To enforce such constraints, we just need to make sure all relevant terms are included in the identified model structure since it can happen that the causation entropy for some but not all of the terms involved

in the constraint is above a given cutoff threshold. Of course, the subsequent parameter estimation is subject to the desired constraints as well, which can be performed using, e.g., the constrained maximum likelihood estimator [28, Section 2.5].

Oftentimes, when constructing ROMs for highly chaotic systems, one needs to include closure terms to take into account the impact of the orthogonal dynamics not resolved by the ROMs [1]. Different strategies can be envisioned to extend the current framework for this purpose. For instance, after the drift part of the causation-based ROM is identified (i.e., the $\Phi(\mathbf{U})$ -term in (6)), instead of fitting the resulting training residual data by a noise term $\sigma\dot{\mathbf{W}}(t)$, we can explore more advanced data-driven techniques such as multilevel approaches and empirical model reduction [48, 49, 59], nonlinear autoregressive techniques [8, 25, 29, 56], or neural networks. Alternatively, one could first learn a higher-dimensional causation-based ROM, then use parameterization techniques [17, 18] to approximate the newly added components by those to be kept.

To what extent one can sparsify a ROM depends apparently on the purposes of the ROMs. However, it can also be tied to the underlying orthogonal basis employed. As already seen in Sec. 3, the causation-based ROMs constructed using the eigenbasis come with a much sparser structure than those built from the POD basis, for the PDE considered. It would be interesting to explore if a coordinate transformation exists that can further enhance the sparsity of the ROMs built on a POD basis. For instance, if we rewrite the POD-ROM under the eigenbasis of the ROM’s linear part, we can oftentimes achieve a diagonalization of the linear terms since eigenvalues with multiplicity one is generic. However, whether this transformation can also help aggregate the nonlinearity to form sparser structures (after re-computing the causation entropy matrix under the transformed basis) is up to further investigation.

Another aspect concerns the efficient computation of the causation entropy matrix when the number of functions, M , in the learning library is in the order of several thousand or beyond, which can, for instance, be encountered for ROMs with dimension 100 or higher. The computational cost for determining a causation entropy lies in the calculation of the log-determinants of the four covariance matrices involved in formula (5), which are of dimension either $M \times M$ or $(M \pm 1) \times (M \pm 1)$. For a ROM of dimension N , there are a total of $N \times M$ causation entropies to determine. Thus, we need to compute the log-determinants of $4 \times N \times M$ covariance matrices, each with dimension about $M \times M$. To gain computational efficiency when M is large, one may benefit from techniques for approximating the log-determinant of a high dimensional symmetric positive definite matrix [10, 65], although additional investigation would be needed to see how one can strike a balance between the computational efficiency gained and the approximation error made on each entry of the causation entropy matrix. Alternatively, we can try to reduce the number of functions in the library by exploring potential physical/modeling insights for the considered applications. For instance, in [28], a localization strategy is introduced to significantly reduce the size of the function library when constructing an efficient causation-based ROM for the two-layer Lorenz 1996 model.

Acknowledgments

This work has been partially funded by the Army Research Office grant W911NF-23-1-0118 (N.C.), the Office of Naval Research grant N00014-24-1-2244 (N.C.), and by the National Science Foundation grants DMS-2108856 and DMS-2407483 (H.L.).

References

- [1] S. E. Ahmed, S. Pawar, O. San, A. Rasheed, T. Iliescu, and B. R. Noack. On closures for reduced order models—A spectrum of first-principle to machine-learned avenues. *Physics of Fluids*, 33(9):091301, 2021.
- [2] A. A. AlMomani and E. Bollt. ERFit: Entropic regression fit MATLAB package, for data-driven system identification of underlying dynamic equations. *arXiv preprint arXiv:2010.02411*, 2020.
- [3] A. A. R. AlMomani, J. Sun, and E. Bollt. How entropic regression beats the outliers problem in nonlinear system identification. *Chaos: An Interdisciplinary Journal of Nonlinear Science*, 30(1), 2020.
- [4] J. Amezcua, K. Ide, E. Kalnay, and S. Reich. Ensemble transform Kalman–Bucy filters. *Quarterly Journal of the Royal Meteorological Society*, 140(680):995–1004, 2014.
- [5] R. E. Bellman. *Dynamic programming treatment of the traveling salesman problem*. RAND Corporation, 1961.
- [6] K. Bergemann and S. Reich. An ensemble Kalman-Bucy filter for continuous data assimilation. *Meteorologische Zeitschrift*, 21:213–219, 2012.
- [7] A. L. Bertozzi and M. C. Pugh. Long-wave instabilities and saturation in thin film equations. *Communications on Pure and Applied Mathematics*, 51:625–661, 1998.
- [8] S. A. Billings. *Nonlinear System Identification: NARMAX Methods in the Time, Frequency, and Spatio-temporal Domains*. John Wiley & Sons, 2013.
- [9] L. Boninsegna, F. Nüske, and C. Clementi. Sparse learning of stochastic dynamical equations. *The Journal of chemical physics*, 148(24), 2018.
- [10] C. Boutsidis, P. Drineas, P. Kambadur, E.-M. Kontopoulou, and A. Zouzias. A randomized algorithm for approximating the log determinant of a symmetric positive definite matrix. *Linear Algebra and its Applications*, 533:95–117, 2017.
- [11] M. Branicki and A. J. Majda. Quantifying uncertainty for predictions with model error in non-Gaussian systems with intermittency. *Nonlinearity*, 25(9):2543, 2012.
- [12] S. L. Brunton, J. L. Proctor, and J. N. Kutz. Discovering governing equations from data by sparse identification of nonlinear dynamical systems. *Proceedings of the National Academy of Sciences*, 113(15):3932–3937, 2016.
- [13] K. Carlberg, C. Farhat, J. Cortial, and D. Amsallem. The GNAT method for nonlinear model reduction: effective implementation and application to computational fluid dynamics and turbulent flows. *Journal of Computational Physics*, 242:623–647, 2013.

- [14] A. Chattopadhyay, M. Mustafa, P. Hassanzadeh, E. Bach, and K. Kashinath. Towards physically consistent data-driven weather forecasting: Integrating data assimilation with equivariance-preserving spatial transformers in a case study with ERA5. *Geoscientific Model Development Discussions*, pages 1–23, 2021.
- [15] A. Chattopadhyay, M. Mustafa, P. Hassanzadeh, and K. Kashinath. Deep spatial transformers for autoregressive data-driven forecasting of geophysical turbulence. In *Proceedings of the 10th International Conference on Climate Informatics*, pages 106–112, 2020.
- [16] A. Chattopadhyay, A. Subel, and P. Hassanzadeh. Data-driven super-parameterization using deep learning: Experimentation with multiscale Lorenz 96 systems and transfer learning. *Journal of Advances in Modeling Earth Systems*, 12(11):e2020MS002084, 2020.
- [17] M. D. Chekroun, H. Liu, and J. C. McWilliams. Variational approach to closure of nonlinear dynamical systems: Autonomous case. *Journal of Statistical Physics*, 179:1073–1160, 2020.
- [18] M. D. Chekroun, H. Liu, and J. C. McWilliams. Stochastic rectification of fast oscillations on slow manifold closures. *Proceedings of the National Academy of Sciences*, 118(48):e2113650118, 2021.
- [19] M. D. Chekroun, H. Liu, and S. Wang. *Stochastic Parameterizing Manifolds and Non-Markovian Reduced Equations: Stochastic Manifolds for Nonlinear SPDEs II*. Springer Briefs in Mathematics, Springer, 2015.
- [20] M. D. Chekroun and D. Kondrashov. Data-adaptive harmonic spectra and multilayer Stuart-Landau models. *Chaos: An Interdisciplinary Journal of Nonlinear Science*, 27(9):093110, 2017.
- [21] M. D. Chekroun, D. Kondrashov, and M. Ghil. Predicting stochastic systems by noise sampling, and application to the El Niño-southern oscillation. *Proceedings of the National Academy of Sciences*, 108(29):11766–11771, 2011.
- [22] N. Chen. Learning nonlinear turbulent dynamics from partial observations via analytically solvable conditional statistics. *Journal of Computational Physics*, 418:109635, 2020.
- [23] N. Chen and Y. Li. BAMCAFE: A Bayesian machine learning advanced forecast ensemble method for complex turbulent systems with partial observations. *Chaos: An Interdisciplinary Journal of Nonlinear Science*, 31(11):113114, 2021.
- [24] N. Chen, Y. Li, and H. Liu. Conditional gaussian nonlinear system: A fast preconditioner and a cheap surrogate model for complex nonlinear systems. *Chaos: An Interdisciplinary Journal of Nonlinear Science*, 32:053122, 2022.
- [25] N. Chen, H. Liu, and F. Lu. Shock trace prediction by reduced models for a viscous stochastic burgers equation. *Chaos: An Interdisciplinary Journal of Nonlinear Science*, 32:043109, 2022.

- [26] N. Chen and A. Majda. Conditional Gaussian systems for multiscale nonlinear stochastic systems: Prediction, state estimation and uncertainty quantification. *Entropy*, 20(7):509, 2018.
- [27] N. Chen and D. Qi. A physics-informed data-driven algorithm for ensemble forecast of complex turbulent systems. *Applied Mathematics and Computation*, 466:128480, 2024.
- [28] N. Chen and Y. Zhang. A causality-based learning approach for discovering the underlying dynamics of complex systems from partial observations with stochastic parameterization. *Physica D: Nonlinear Phenomena*, 449:133743, 2023.
- [29] A. J. Chorin and F. Lu. Discrete approach to stochastic parametrization and dimension reduction in nonlinear dynamics. *Proceedings of the National Academy of Sciences*, 112(32):9804–9809, 2015.
- [30] A. Cortiella, K.-C. Park, and A. Doostan. Sparse identification of nonlinear dynamical systems via reweighted ℓ_1 -regularized least squares. *Computer Methods in Applied Mechanics and Engineering*, 376:113620, 2021.
- [31] T. M. Cover. *Elements of information theory*. John Wiley & Sons, 1999.
- [32] D. Crommelin and A. Majda. Strategies for model reduction: Comparing different optimal bases. *J. Atmos. Sci.*, 61(17):2206–2217, 2004.
- [33] J. Elinger. *Information Theoretic Causality Measures For Parameter Estimation and System Identification*. PhD thesis, Georgia Institute of Technology, Atlanta, GA, USA, 2021.
- [34] J. Elinger and J. Rogers. Causation entropy method for covariate selection in dynamic models. In *2021 American Control Conference (ACC)*, pages 2842–2847. IEEE, 2021.
- [35] J. Fish, A. DeWitt, A. A. R. AlMomani, P. J. Laurienti, and E. Boltt. Entropic regression with neurologically motivated applications. *Chaos: An Interdisciplinary Journal of Nonlinear Science*, 31(11), 2021.
- [36] M. Ghil and S. Childress. *Topics in geophysical fluid dynamics: atmospheric dynamics, dynamo theory, and climate dynamics*. Springer Science & Business Media, 2012.
- [37] A. Hannachi, I. T. Jolliffe, and D. B. Stephenson. Empirical orthogonal functions and related techniques in atmospheric science: A review. *Int. J. Climatol.*, 27:1119–1152, 2007.
- [38] J. Harlim, A. Mahdi, and A. J. Majda. An ensemble Kalman filter for statistical estimation of physics constrained nonlinear regression models. *Journal of Computational Physics*, 257:782–812, 2014.
- [39] K. Hasselmann. PIPs and POPs: The reduction of complex dynamical systems using principal interaction and oscillation patterns. *Journal of Geophysical Research: Atmospheres*, 93(D9):11015–11021, 1988.
- [40] S. Hijazi, G. Stabile, A. Mola, and G. Rozza. Data-driven pod-galerkin reduced order model for turbulent flows. *Journal of Computational Physics*, 416:109513, 2020.

- [41] P. Holmes, J. L. Lumley, and G. Berkooz. *Turbulence, Coherent Structures, Dynamical Systems and Symmetry*. Cambridge, 1996.
- [42] P. Holmes, J. L. Lumley, G. Berkooz, and C. W. Rowley. *Turbulence, Coherent Structures, Dynamical Systems and Symmetry*. Cambridge University Press, Cambridge, second edition, 2012.
- [43] J. M. Hyman, B. Nicolaenko, and S. Zaleski. Order and complexity in the Kuramoto-Sivashinsky model of weakly turbulent interfaces. *Physica D*, 23:265–292, 1986.
- [44] M. Jardak, I. Navon, and M. Zupanski. Comparison of sequential data assimilation methods for the Kuramoto–Sivashinsky equation. *International Journal for Numerical Methods in Fluids*, 62:374–402, 2010.
- [45] A. Kassam and L. N. Trefethen. Fourth-order time-stepping for stiff PDEs. *SIAM J. Sci. Comp.*, 26(4):1214–1233, 2005.
- [46] P. Kim, J. Rogers, J. Sun, and E. Bollt. Causation entropy identifies sparsity structure for parameter estimation of dynamic systems. *Journal of Computational and Nonlinear Dynamics*, 12(1):011008, 2017.
- [47] R. Kleeman. Information theory and dynamical system predictability. *Entropy*, 13(3):612–649, 2011.
- [48] D. Kondrashov, M. D. Chekroun, and M. Ghil. Data-driven non-Markovian closure models. *Physica D: Nonlinear Phenomena*, 297:33–55, 2015.
- [49] S. Kravtsov, D. Kondrashov, and M. Ghil. Multilevel regression modeling of nonlinear processes: Derivation and applications to climatic variability. *Journal of Climate*, 18(21):4404–4424, 2005.
- [50] Y. Kuramoto and T. Tsuzuki. Persistent propagation of concentration waves in dissipative media far from thermal equilibrium. *Prog. Theor. Phys.*, 55(2):356–369, 1976.
- [51] F. Kwasniok. The reduction of complex dynamical systems using principal interaction patterns. *Physica D: Nonlinear Phenomena*, 92(1-2):28–60, 1996.
- [52] F. Kwasniok. Optimal Galerkin approximations of partial differential equations using principal interaction patterns. *Physical Rev. E*, 55(5):5365, 1997.
- [53] R. LaQuey, S. Mahajan, P. Rutherford, and W. Tang. Nonlinear saturation of the trapped-ion mode. *Physical Review Letters*, 34:391–394, 1975.
- [54] A. Larios and Y. Pei. Nonlinear continuous data assimilation. *Evolution Equations and Control Theory*, 13:329–348, 2024.
- [55] K. K. Lin and F. Lu. Data-driven model reduction, wiener projections, and the Koopman-Mori-Zwanzig formalism. *Journal of Computational Physics*, 424:109864, 2021.

- [56] F. Lu, K. K. Lin, and A. J. Chorin. Data-based stochastic model reduction for the Kuramoto–Sivashinsky equation. *Physica D: Nonlinear Phenomena*, 340:46–57, 2017.
- [57] E. Lunasin and E. S. Titi. Finite determining parameters feedback control for distributed nonlinear dissipative systems – a computational study. *Evolution Equations and Control Theory*, 6:535–557, 2017.
- [58] A. J. Majda and N. Chen. Model error, information barriers, state estimation and prediction in complex multiscale systems. *Entropy*, 20(9):644, 2018.
- [59] A. J. Majda and J. Harlim. Physics constrained nonlinear regression models for time series. *Nonlinearity*, 26(1):201, 2012.
- [60] A. Moosavi, R. Stefanescu, and A. Sandu. Efficient construction of local parametric reduced order models using machine learning techniques. *arXiv preprint arXiv:1511.02909*, 2015.
- [61] C. Mou, B. Koc, O. San, L. G. Rebholz, and T. Iliescu. Data-driven variational multiscale reduced order models. *Computer Methods in Applied Mechanics and Engineering*, 373:113470, 2021.
- [62] C. Mou, L. M. Smith, and N. Chen. Combining stochastic parameterized reduced-order models with machine learning for data assimilation and uncertainty quantification with partial observations. *Journal of Advances in Modeling Earth Systems*, 15(10):e2022MS003597, 2023.
- [63] B. R. Noack, M. Morzynski, and G. Tadmor. *Reduced-order modelling for flow control*, volume 528. Springer Science & Business Media, 2011.
- [64] S. E. Otto and C. W. Rowley. Linearly recurrent autoencoder networks for learning dynamics. *SIAM Journal on Applied Dynamical Systems*, 18:558–593, 2019.
- [65] R. K. Pace and J. P. LeSage. A sampling approach to estimate the log determinant used in spatial likelihood problems. *Journal of Geographical Systems*, 11(3):209–225, 2009.
- [66] S. Pawar, S. E. Ahmed, O. San, and A. Rasheed. Data-driven recovery of hidden physics in reduced order modeling of fluid flows. *Physics of Fluids*, 32(3):036602, 2020.
- [67] B. Peherstorfer and K. Willcox. Dynamic data-driven reduced-order models. *Computer Methods in Applied Mechanics and Engineering*, 291:21–41, 2015.
- [68] C. Penland and T. Magorian. Prediction of Niño 3 sea surface temperatures using linear inverse modeling. *Journal of Climate*, 6:1067–1076, 1993.
- [69] C. W. Rowley, I. Mezić, S. Bagheri, P. Schlatter, and D. S. Henningson. Spectral analysis of nonlinear flows. *Journal of Fluid Mechanics*, 641:115–127, 2009.
- [70] O. San and R. Maulik. Extreme learning machine for reduced order modeling of turbulent geophysical flows. *Physical Review E*, 97(4):042322, 2018.

- [71] F. Santosa and W. W. Symes. Linear inversion of band-limited reflection seismograms. *SIAM Journal on Scientific and Statistical Computing*, 7(4):1307–1330, 1986.
- [72] H. Schaeffer, G. Tran, and R. Ward. Extracting sparse high-dimensional dynamics from limited data. *SIAM Journal on Applied Mathematics*, 78(6):3279–3295, 2018.
- [73] P. J. Schmid. Dynamic mode decomposition of numerical and experimental data. *Journal of Fluid Mechanics*, 656:5–28, 2010.
- [74] T. Schneider, A. M. Stuart, and J.-L. Wu. Learning stochastic closures using ensemble Kalman inversion. *Transactions of Mathematics and Its Applications*, 5(1):tnab003, 2021.
- [75] S. A. Sheard and A. Mostashari. Principles of complex systems for systems engineering. *Systems Engineering*, 12(4):295–311, 2009.
- [76] L. Sirovich. Turbulence and the dynamics of coherent structures. Parts I–III. *Quart. Appl. Math.*, 45(3):561–590, 1987.
- [77] G. Sivashinsky. Nonlinear analysis of hydrodynamic instability in laminar flames-I. Derivation of basic equations. *Acta Astronautica*, 4(11-12):1177–1206, 1977.
- [78] G. I. Sivashinsky and D. M. Michelson. On irregular wavy flow of a liquid film down a vertical plane. *Progress of theoretical physics*, 63:2112–2114, 1980.
- [79] F. Smarra, A. Jain, T. De Rubeis, D. Ambrosini, A. D’Innocenzo, and R. Mangharam. Data-driven model predictive control using random forests for building energy optimization and climate control. *Applied energy*, 226:1252–1272, 2018.
- [80] K. Srinivasan, M. D. Chekroun, and J. C. McWilliams. Turbulence closure with small, local neural networks: Forced two-dimensional and β -plane flows. *Journal of Advances in Modeling Earth Systems*, 16:e2023MS003795, 2024.
- [81] P. Stinis. Stochastic optimal prediction for the Kuramoto–Sivashinsky equation. *Multiscale Model. Simul.*, 2(4):580–612, 2004.
- [82] S. H. Strogatz. *Nonlinear dynamics and chaos with student solutions manual: With applications to physics, biology, chemistry, and engineering*. CRC press, 2018.
- [83] K. Taira, S. L. Brunton, S. T. M. Dawson, C. W. Rowley, T. Colonius, B. J. McKeon, O. T. Schmidt, S. Gordeyev, V. Theofilis, and L. S. Ukeiley. Modal analysis of fluid flows: An overview. *AIAA Journal*, 55:4013–4041, 2017.
- [84] K. Taira, M. S. Hemati, S. L. Brunton, Y. Sun, K. Duraisamy, S. Bagheri, S. T. Dawson, and C.-A. Yeh. Modal analysis of fluid flows: Applications and outlook. *AIAA journal*, 58(3):998–1022, 2020.
- [85] R. Tibshirani. Regression shrinkage and selection via the lasso. *Journal of the Royal Statistical Society: Series B (Methodological)*, 58(1):267–288, 1996.

- [86] M. K. Tippett, R. Kleeman, and Y. Tang. Measuring the potential utility of seasonal climate predictions. *Geophysical research letters*, 31(22), 2004.
- [87] J. H. Tu, C. W. Rowley, D. M. Luchtenburg, S. L. Brunton, and J. N. Kutz. On dynamic mode decomposition: Theory and applications. *Journal of Computational Dynamics*, 1:391–421, 2014.
- [88] G. K. Vallis. *Atmospheric and oceanic fluid dynamics*. Cambridge University Press, 2017.
- [89] Z. Y. Wan and T. P. Sapsis. Reduced-space Gaussian process regression for data-driven probabilistic forecast of chaotic dynamical systems. *Physica D: Nonlinear Phenomena*, 345:40–55, 2017.
- [90] D. C. Wilcox. Multiscale model for turbulent flows. *AIAA journal*, 26(11):1311–1320, 1988.
- [91] M. Williams, I. Kevrekidis, and C. Rowley. A data-driven approximation of the Koopman operator: Extending dynamic mode decomposition. *Journal of Nonlinear Science*, 25(6):1307–1346, 2015.
- [92] X. Xie, M. Mohebbujaman, L. G. Rebholz, and T. Iliescu. Data-driven filtered reduced order modeling of fluid flows. *SIAM Journal on Scientific Computing*, 40(3):B834–B857, 2018.
- [93] X. Ying. An overview of overfitting and its solutions. In *Journal of physics: Conference series*, volume 1168, page 022022. IOP Publishing, 2019.